ATLAS NOTE

ATLAS-CONF-2013-012

March 5, 2013

Measurements of the properties of the Higgs-like boson in the two photon decay channel with the ATLAS detector using 25 fb^{-1} of proton-proton collision data

The ATLAS Collaboration

Abstract

Measurements of the mass and couplings of the Higgs-like boson in the two photon decay channel with the ATLAS detector at the LHC are presented. The proton-proton collision datasets used correspond to integrated luminosities of 4.8 fb^{-1} collected at $\sqrt{s}$ = 7 TeV and 20.7 fb^{-1} collected at $\sqrt{s}$ = 8 TeV. The updated measurements benefit from an increased data sample and an improved analysis. The measured value of the mass of the Higgs-like boson is $126.8 \pm 0.2(\text{stat}) \pm 0.7(\text{syst})$ GeV and the fitted number of signal events is found to be $1.65 \pm 0.24(\text{stat})^{+0.25}_{-0.18}(\text{syst})$ times the value predicted by the Standard Model. Measurements of the signal strengths in different production processes and a fiducial cross section for the observed particle are also presented.

ATLAS-CONF-2013-012
06 March 2013

1 Introduction

According to the Standard Model (SM) of particle physics, elementary particles acquire their mass through a mechanism that spontaneously breaks the electroweak symmetry. A consequence of this model is the existence of a scalar particle, the SM Higgs boson [1–3]. In July 2012, the ATLAS and CMS collaborations independently reported observations of a new particle that seems compatible with the SM Higgs boson, using pp collisions from the 2011 and 2012 datasets collected at the LHC until the end of June 2012 [4, 5]. More detailed and precise measurements of the properties of this new boson are essential to further elucidate its role in electroweak symmetry breaking and mass generation.

The results of the previous ATLAS Higgs boson searches and property measurements in the diphoton decay channel were obtained with a combination of 4.8 fb^{-1} of data recorded at $\sqrt{s} = 7$ TeV and 13.0 fb^{-1} of data recorded at $\sqrt{s} = 8$ TeV [6]. They established the observation of the new boson in the diphoton channel alone.

The results reported here are obtained from the whole data sample collected in 2012 at $\sqrt{s} = 8$ TeV, enlarged to a total of 20.7 fb^{-1} by including data recorded between October and December 2012. The analysis strategy has been improved to be more sensitive to different signal production processes allowing a more precise measurement of their strengths. The mass measurement is also updated with the full 2012 dataset and a first measurement of the fiducial cross section of the new particle is presented. The 8 TeV analysis is combined with the previous 7 TeV analysis, which is unchanged with respect to Ref. [6].

This note is organised as follows: the ATLAS detector is briefly described in Section 2, followed by the event selection, object selection and event categorisation in Sections 3 and 4. The signal and background modelling are presented in Section 5. Systematic uncertainties are summarised in Section 6. The statistical procedures and the results of the combination of the $\sqrt{s} = 7$ TeV and $\sqrt{s} = 8$ TeV data are discussed in Section 7. The conclusions of this study are reported in Section 8.

2 The ATLAS detector

The ATLAS detector [7] is a multipurpose apparatus with a forward-backward symmetric cylindrical geometry with close to 4π coverage in solid angle[1].

The inner tracking detector (ID), covering a pseudo-rapidity range of $|\eta| < 2.5$, consists of a silicon pixel detector, a silicon microstrip detector and a transition radiation tracker in the range $|\eta| < 2.0$. The ID is surrounded by a superconducting solenoid providing a 2 T magnetic field. The inner detector allows an accurate reconstruction of the primary proton-proton collision region, as well as tracks from secondary vertices, thus permitting an efficient reconstruction of tracks from photons converting into an electron-positron pair in the inner detector material up to a radius of ~ 800 mm.

The electromagnetic (EM) calorimeter (ECAL) provides a measurement of the kinematics of EM objects. It is a lead/liquid-argon (LAr) sampling calorimeter with an accordion geometry. The ECAL is divided into a barrel section, covering the pseudorapidity region $|\eta| < 1.475$, and two end-cap sections, covering the pseudorapidity regions $1.375 < |\eta| < 3.2$. It consists of three longitudinal layers up to $|\eta| = 2.5$ and two layers in the rest of the coverage. The first one is segmented, in the ranges $|\eta| < 1.4$ and $1.5 < |\eta| < 2.4$, into high granularity "strips" in the η direction, sufficient to provide an event-by-event discrimination between single photon showers and two overlapping showers generated by the decay of a π^0 meson. The second layer collects most of the energy deposited by a photon shower. A third layer is

[1] ATLAS uses a right-handed coordinate system with its origin at the nominal interaction point (IP) in the centre of the detector, and the z-axis along the beam line. The x-axis points from the IP to the centre of the LHC ring, and the y-axis points upwards. Cylindrical coordinates (r, φ) are used in the transverse plane, φ being the azimuthal angle around the beam line. Observables labelled "transverse" are projected into the $x - y$ plane. The pseudorapidity is defined in terms of the polar angle θ as $\eta = -\ln\tan(\theta/2)$. The transverse momentum is defined as $p_T = p\sin\theta = p\,/\cosh\eta$, and the transverse energy E_T has a similar definition.

used to correct leakage beyond the ECAL for high energy showers. In front of the accordion calorimeter a thin presampler layer, covering the pseudorapidity interval $|\eta| < 1.8$, is used to correct for energy losses before the calorimeter.

The hadronic calorimeter (HCAL), surrounding the ECAL, consists of steel and scintillating tiles in the range $|\eta| < 1.7$, and two copper/LAr detectors spanning $1.5 < |\eta| < 3.2$. The acceptance is extended by two copper-tungsten/LAr forward calorimeters up to $|\eta| < 4.9$.

The muon spectrometer, located beyond the calorimeters, consists of three large air-core superconducting toroid systems, precision tracking chambers providing accurate muon tracking over $|\eta| < 2.7$, and fast detectors for triggering over $|\eta| < 2.4$.

A three-level trigger system is used to select events containing two photon candidates. The first level trigger is hardware based and exploits a coarse cell granularity (0.1×0.1 in $\eta \times \varphi$) to search for electromagnetic deposits with transverse energies above a programmable threshold. The second and third level triggers are implemented in software and exploit the full granularity and energy calibration of the calorimeter.

3 Event selection

The data sample was recorded with a diphoton trigger with 35 GeV and 25 GeV transverse energy (E_{T}) thresholds for the leading (highest E_{T}) and sub-leading photons, respectively. The trigger uses clusters of energy in the EM calorimeter. At the final trigger level these EM clusters are required to match loose criteria according to expectations for EM showers initiated by photons. This trigger has a signal efficiency above 99% for events fulfilling the final event selection. After application of data quality requirements, the 8 TeV data sample corresponds to a total integrated luminosity of 20.7 ± 0.7 fb^{-1}.

In the offline event selection at least two photons satisfying tight identification criteria based on the shapes of the EM showers [8] are required. The transverse energies for the leading and sub-leading photons are required to be larger than 40 GeV and 30 GeV, respectively, and both need to be within the fiducial calorimeter region of $|\eta| < 2.37$ (excluding the transition region between the barrel and the end-cap calorimeters, $1.37 < |\eta| < 1.56$). The photon identification efficiency for the tight criteria is typically 85% at low E_{T} and reaches a plateau of 95% around $E_{\mathrm{T}} = 100$ GeV.

Both photons are also required to be isolated through the use of criteria based on both the inner tracker and the calorimeter. The first is the scalar sum of the transverse momenta of all tracks with $p_{\mathrm{T}} > 1$ GeV in a cone of size $\Delta R = \sqrt{(\Delta\eta)^2 + (\Delta\varphi)^2} = 0.2$ around each photon, and is required to be less than 2.6 GeV. Only tracks consistent with originating from the diphoton production vertex (its selection is outlined below) are used, and tracks associated to converted photon candidates are excluded. The second variable is the transverse energy sum of positive-energy topological clusters [9] deposited in the calorimeter around each photon in a cone of $\Delta R = 0.4$, and is required to be less than 6 GeV. The energy sum excludes deposits in in the core region of the photon shower, and corrections for the small estimated energy leakage outside this region are applied. The effects of the underlying event and of additional minimum bias interactions (pile-up) occurring in the same or neighbouring bunch crossings are corrected on an event-by-event basis [10, 11].

For the precise measurement of the diphoton invariant mass ($m_{\gamma\gamma}$), as well as for the computation of track-based quantities (e.g. track isolation, selection of jets associated to the hard interaction), the precise location of the diphoton production vertex is necessary. The determination of this vertex is based on the so-called 'photon pointing', where the vertex position along the beam axis is obtained by combining the trajectories of each photon, measured using the longitudinal segmentation of the calorimeter, with a constraint from the average beam spot position. For converted photons, the position of the conversion vertex is also used if tracks from the conversion have hits in the silicon detectors. The diphoton production vertex is selected among all the reconstructed primary vertices using a Neural Network algorithm which

combines the photon pointing with, for each reconstructed vertex: the conversion information, the sum of the squared momentum $\sum p_{\mathrm{T}}^2$ and the scalar sum of the momentum $\sum p_{\mathrm{T}}$ of the tracks associated with each reconstructed vertex, and the difference in azimuthal angle $\Delta\varphi$ between the direction defined by the vector sum of the tracks momenta and that of the diphoton system. The vertex selection was studied with $Z \to ee$ events in data and Monte Carlo (MC) simulation by removing the electron tracks from the events and verifying the efficiency of finding the vertex associated to them. Corrections were applied in order to mimic the Higgs boson signal, by matching the dielectron and diphoton p_{T} spectra in the MC and the fraction of events with zero, one or two EM objects in the barrel region of the calorimeter. The efficiency of finding the primary vertex within 0.3 mm of the true one is higher than 75%.

The photon energy calibration is obtained from a detailed simulation of the detector geometry and response independently for converted and unconverted photons. For the purpose of calibration, converted photons are defined as those with a conversion vertex reconstructed in the inner detector at a radius of less than 800 mm, and tracks matched to the calorimeter cluster. The calibration is refined by applying η-dependent correction factors determined in situ. These go from ±0.5% to ±1.5% depending on the pseudorapidity of the photon and are obtained from studies of $Z \to ee$ decays in data [12]. The energy response of the calorimeter shows a stability within 0.1% with time and with different pile-up conditions, the mean number of interactions per bunch crossing for 2012 being around 20, and spanning up to 40.

A total of 118893 (23788) collisions events at 8 TeV (7 TeV) were selected with a diphoton invariant mass between 100 GeV and 160 GeV. Using methods based on photon identification quality and isolation [13], the fraction of genuine diphoton events is found to be $(75^{+3}_{-4})\%$ [6]. The rest of the events contain one or more jets misidentified as photons, except for a small contribution from the Drell-Yan process where both electrons pass the photon selection. Conversion candidates with tracks crossing inactive regions of the innermost pixel layer are rejected to reduce the contamination from misidentified electrons. The study of the sample composition demonstrates the high purity of the diphoton selection, although the Higgs boson analysis and properties measurements do not rely on the determination of the background composition.

4 Event categorisation

The selected events are divided into 14 exclusive categories based on event properties. The categories differ in signal-to-background ratio as well as invariant mass resolution and thus increase the sensitivity of the measurement. Gluon fusion (ggF) is the dominant production mode of Higgs bosons at the LHC, contributing 87% of the total production cross section at $m_H = 126.5$ GeV, while vector boson fusion (VBF) and associated production with vector bosons (VH) contribute only 7% and 5% respectively. Several categories are designed to increase the sensitivity to the VBF and VH processes. An order of preference is applied when sorting events into categories (Figure 1). Compared to the previous analysis [6], new categories enriched in associated production with vector bosons have been introduced and a multivariate analysis is performed to improve the sensitivity to the VBF production mode. The selection of the different objects needed to define the categories are described in this section, followed by the description of the categories.

4.1 Object selection

4.1.1 Leptons

Electron candidates are reconstructed from clusters of energy deposits in the electromagnetic calorimeter associated with a track reconstructed in the inner detector. A transverse energy greater than 15 GeV and $|\eta| < 2.47$ are required. Identification criteria based on electromagnetic shower shapes and track quality are applied [12]; shower shapes criteria are similar to but somewhat looser than those for photons.

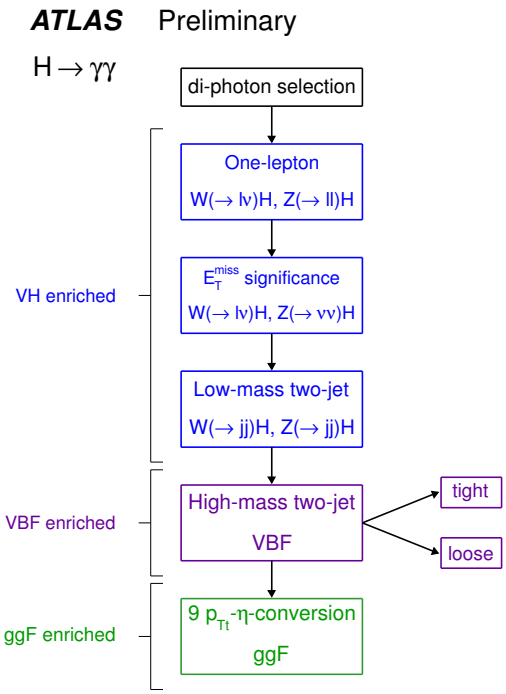

Figure 1: Flow-chart of the event categorisation, giving the order of selection of the different categories.

Muon candidates are reconstructed from tracks in the inner detector and the muon spectrometer, and in the forward region ($2.5 < |\eta| < 2.7$) from the muon spectrometer alone. A transverse momentum larger than 10 GeV is required.

Both electron and muon candidates are required to be isolated in the tracker and calorimeter with algorithms similar to the photon isolation requirements. The track-isolation divided by the total muon p_{T} (electron E_{T}) is required to be less than 0.15 and the calorimetric isolation divided by the total muon p_{T} (electron E_{T}) is required to be less than 0.2.

4.1.2 Jets

Jets are reconstructed from three-dimensional clusters of energy in the electromagnetic and hadronic calorimeters using the anti-k_t algorithm [14] with a distance parameter of $R = 0.4$. Jet candidates are required to have a transverse energy greater than 25 GeV (30 GeV) for $|\eta^{\mathrm{jet}}| < 2.4$ ($2.4 \leq |\eta^{\mathrm{jet}}| < 4.5$). The energy dependence on the additional interactions in the same bunch crossing (in-time pile-up), as well as from multiple interactions in surrounding bunch crossings (out-of-time pile-up), is mitigated by applying a data-driven correction based on the event p_{T} density in the jet area [11]. Corrections from in-situ measurements are then applied to refine the jet calibration [15]. To remove jets originating from pile-up interactions, jets with $|\eta^{\mathrm{jet}}| \leq 2.4$ and $p_{\mathrm{T}} < 50$ GeV [2] must fulfil the requirement, based on tracking information, that they originate from the diphoton production vertex. A jet vertex fraction (JVF) is calculated for each primary vertex using tracks associated to the jet and is defined as the ratio of the p_{T} sum of the jet tracks associated to the selected vertex and the p_{T} sum of all jet tracks. The JVF for the primary vertex selected in the analysis is required to be greater than 0.25. The efficiency of selecting the

[2] Jets with $p_{\mathrm{T}} > 50$ GeV have a small probability to be produced by pile-up interactions.

correct jets from VBF $H \to \gamma\gamma$ events is larger than 95% with this cut. The two highest p_{T} jets passing all the jet selection cuts are used for the categorisation.

To prevent potential double-counting, the reconstructed objects are required to have a minimal spatial separation. The two leading photons are always kept. Electrons overlapping with one of those photons within a cone of $\Delta R(e,\gamma) = \sqrt{\Delta\eta^2 + \Delta\varphi^2} < 0.4$, jets within $\Delta R(\mathrm{jet}, e) < 0.2$ or $\Delta R(\mathrm{jet}, \gamma) < 0.4$, and muons within a cone of $\Delta R(\mu, \mathrm{jet}) < 0.4$ or $\Delta R(\mu, \gamma) < 0.4$ are removed.

4.1.3 Missing transverse energy

The measurement of the missing transverse energy, $E_{\mathrm{T}}^{\mathrm{miss}}$, is based on the transverse energy of all photon, electron and muon candidates, all jets after overlap removal, and all calorimeter energy clusters not associated to such objects. The objects entering the $E_{\mathrm{T}}^{\mathrm{miss}}$ definition are selected with the criteria described above.

The $E_{\mathrm{T}}^{\mathrm{miss}}$ significance is defined as $E_{\mathrm{T}}^{\mathrm{miss}}/\sigma_{E_{\mathrm{T}}^{\mathrm{miss}}}$ where $\sigma_{E_{\mathrm{T}}^{\mathrm{miss}}} = 0.67\ [\ \mathrm{GeV}^{1/2}]\ \sqrt{\Sigma E_{\mathrm{T}}}$, ΣE_{T} being the scalar sum of the transverse energy of all objects [16]. Using a $E_{\mathrm{T}}^{\mathrm{miss}}$ significance requirement instead of a direct $E_{\mathrm{T}}^{\mathrm{miss}}$ requirement allows the rejection of multijet events where the $E_{\mathrm{T}}^{\mathrm{miss}}$ arises from energy resolution effects, while still retaining high efficiency for signal events with $E_{\mathrm{T}}^{\mathrm{miss}}$ coming from particles which do not interact with the detector.

4.2 Categories sensitive to the associated production with a vector boson

In the first step of the categorisation, events with with features expected from the associated production of the Higgs particle with a vector boson are selected. Categories are described in the order they are selected.

4.2.1 One-lepton category

Events where the vector boson decays leptonically are sought by identifying either an electron or a muon candidate. In order to remove the background coming from the $Z(\to ee)\gamma$ process, events having $84 < m_{e\gamma} < 94$ GeV, where $m_{e\gamma}$ is the diphoton mass of the reconstructed electron and one of the two photons, are vetoed. If one of the selected photons also passes the electron identification requirements, the event is rejected to reduce the background from electroweak processes, particularly from $W(\to e\nu)\gamma$ where the electron is misidentified as a photon.

4.2.2 $E_{\mathrm{T}}^{\mathrm{miss}}$ significance category

In order to select Z bosons decaying into two neutrinos or W bosons decaying leptonically but with a lepton which was not reconstructed, events with a $E_{\mathrm{T}}^{\mathrm{miss}}$ significance larger than 5 are selected, which corresponds to $E_{\mathrm{T}}^{\mathrm{miss}} > 70-100$ GeV depending on ΣE_{T}. Events with at least one photon passing electron identification requirements are also rejected from this category to reduce the electroweak background.

4.2.3 Low mass two-jet category

Events with a signature of hadronically decaying vector bosons are found by requiring the presence of two reconstructed jets with a dijet invariant mass in the range of 60-110 GeV and a pseudorapidity separation between the two jets of less than 3.5 units. The difference between the pseudorapidities of the diphoton and the dijet systems is required to be lower than 1. In addition, the diphoton transverse

momentum orthogonal to the diphoton thrust axis in the transverse plane [3] (p_{Tt}) [17, 18] is required to be larger than 70 GeV.

4.3 Categories sensitive to the vector boson fusion process

Vector-boson fusion events are characterised by two forward jets with little hadronic activity between the two jets. A multivariate analysis is performed to improve the sensitivity to this process. It exploits the full event topology and the correlations of jets and photons kinematic quantities to maximize the discrimination of the VBF signal from the relevant backgrounds, which include: non-resonant processes such as $\gamma\gamma$ pairs produced in association with at least two jets, direct single γ events with at least three jets (with one jet faking a photon) and multi-jet events where two jets are misidentified as photons, as well as resonant backgrounds such as Higgs bosons production via gluon fusion and in association with at least two jets. Eight discriminating variables are used to build a boosted decision tree (BDT) [19]: the invariant mass of the two leading jets m_{jj}, their pseudorapidity η_{j1} and η_{j2}, their pseudorapidity separation $\Delta\eta_{jj}$, p_{Tt} of the diphoton system, the azimuthal angle difference between the diphoton and the dijet systems $\Delta\phi_{\gamma\gamma;jj}$, the diphoton system pseudorapidity in the frame of the tagging jet pseudorapidity, defined as $\eta^* = \eta_{\gamma\gamma} - \frac{\eta_{j1}+\eta_{j2}}{2}$ [20], and the minimal ΔR between one of the photons and one of the two leading jets $\Delta R^{\gamma j}_{\mathrm{min}}$.

For the BDT training, a Monte Carlo sample generated with Sherpa is used to emulate the diphoton component of the background while data events in which one of the photon candidates fails the isolation criteria are used to emulate the photon-jet and two-jet components of the background. Each component is weighted according to the background composition measured in data. The BDT responses to the data excluding the signal region (sidebands) and to the expected background are shown in Figure 2(a).

Two categories are defined according to the BDT output value, leading to tight (BDT ≥ 0.74) and loose ($0.44 <$ BDT < 0.74) "high-mass two-jet" categories. They are determined by maximizing the VBF signal significance against ggF and non-resonant backgrounds using a statistically independent subset of the training sample. Figure 2(b) shows the BDT response for the non-resonant background, and the ggF and VBF samples. A clear separation between the VBF signal and the other processes can be seen.

Although to derive the final results the background is not obtained from the MC simulation, the distributions of the BDT input variables in the data sidebands and in the training sample were compared before and after the cuts on the BDT output value. They were found to be in reasonable agreement. To further check the performance of the BDT, the output for a high statistics, high purity, $Z \to ee$ + jet sample was compared between data and MC. A good agreement was observed over the full range of the BDT output. The diphoton MC sample at the generator level was used to verify that the shape of the diphoton invariant mass spectrum is not affected by the cuts on the BDT discriminant.

4.4 Other categories

The remaining events are classified by whether both photon candidates are unconverted photons ("unconverted") or at least one photon candidate is a converted photon ("converted"), whether both photon candidates are within $|\eta| < 0.75$ ("central") or at least one photon candidate is outside of this region ("rest"), and whether the p_{Tt} of the diphoton system is greater ("high-p_{Tt}") or smaller ("low-p_{Tt}") than 60 GeV. For events with at least one converted photon candidate, a separate "converted transition" category is defined, where at least one photon candidate has $1.3 < |\eta| < 1.75$. The energy resolution

[3] $p_{\mathrm{Tt}} = |\vec{p}^{\,\gamma\gamma}_{\mathrm{T}} \times \widehat{t}|$, where $\widehat{t} = \frac{\vec{p}^{\,\gamma 1}_{\mathrm{T}} - \vec{p}^{\,\gamma 2}_{\mathrm{T}}}{|\vec{p}^{\,\gamma 1}_{\mathrm{T}} - \vec{p}^{\,\gamma 2}_{\mathrm{T}}|}$ denotes the transverse thrust, $\vec{p}^{\,\gamma 1}_{\mathrm{T}}$ and $\vec{p}^{\,\gamma 2}_{\mathrm{T}}$ are the transverse momenta of the two photons, and $\vec{p}^{\,\gamma\gamma}_{\mathrm{T}} = \vec{p}^{\,\gamma 1}_{\mathrm{T}} + \vec{p}^{\,\gamma 2}_{\mathrm{T}}$ is the transverse momentum of the diphoton system.

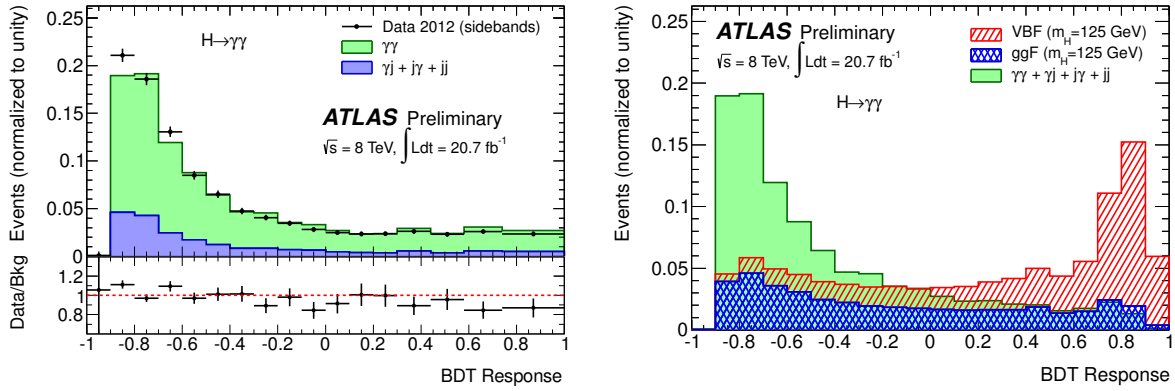

(a) (b)

Figure 2: (a) The response of the VBF BDT to the data in the signal sidebands (excluding the $m_{\gamma\gamma} \in$ [120-130] GeV region) and to the expected background after selection cuts, normalized to unity. (b) The response of the VBF BDT to the VBF signal sample, to the ggF signal sample, and to the expected background after selection cuts, normalized to unity.

is degraded in this region because of the large amount of material in front of the calorimeter. No p_{Tt} classification is applied to this last category.

5 Signal and background modelling

5.1 Signal modelling

The Higgs boson signal produced through the gluon fusion and vector boson fusion processes is simulated with the Powheg [21, 22] generator interfaced to Pythia [23] for showering and hadronisation. Higgs boson production in association with a vector boson or a top quark pair (ttH) is simulated with Pythia. The Higgs boson production cross sections are computed up to next-to-next-to-leading order (NNLO) [24–29] in QCD for the gluon fusion process. Soft-gluon resummation up to next-to-next-to-leading logarithm order [30] is adopted. The finite quark-mass effects are taken into account in Powheg [31]. Next-to-leading order (NLO) EW corrections are applied [32, 33]. These results are compiled in [34–36] assuming factorization between QCD and EW corrections. The cross sections for the VBF process are calculated with full NLO QCD and EW corrections [37–39], and approximate NNLO QCD corrections [40]. The W/ZH processes are calculated at NLO [41] and NNLO [42], and NLO EW radiative corrections [43] are applied. The full NLO QCD corrections for ttH are used [44–47].

The yields for gluon fusion are, in the following, corrected for destructive interference with the $gg \rightarrow \gamma\gamma$ process [48]. These corrections range between -2% and -5%, depending on the diphoton invariant mass.

The theoretical uncertainty on the Higgs boson production cross section mainly comes from renormalisation and factorisation scale variations and parton distribution functions (PDF) [49–52]. The Higgs boson decay branching fractions are taken from Refs. [53–56] and their uncertainties are compiled in Refs. [57, 58].

Signal MC samples are generated in steps of 5 GeV for hypothesised Higgs boson masses in the range 100-150 GeV and passed through a full ATLAS detector simulation [59] based on the GEANT4 program [60]. Pile-up effects are simulated by overlaying each MC event with a number of additional simulated inelastic pp collisions. The number of extra interactions is adjusted according to the measured

multiplicity in each data-taking period. In the simulation, the photon energy resolution is broadened (by approximately 1% in the barrel calorimeter and 1.5-2.5% in the end-cap regions) to account for differences in energy resolution observed between $Z \to ee$ data and MC events. In the pseudorapidity region $0.8-1.37$, the energy resolution broadening applied for the 2012 analysis is larger due to aditionnal differences between data and simulation for the $Z \to ee$ invariant mass distribution. This broadens the predicted diphoton mass resolution, which is based on the resolution extracted from $Z \to ee$ events, and increases its uncertainty.

A Crystal Ball [61] plus a Gaussian function is used to describe the diphoton invariant mass distribution from the signal MC samples. The parameters of this function, as well as the signal yield, are parameterised as a function of hypothesised Higgs boson mass, and a simultaneous fit to signal MC samples at different masses is performed to interpolate the signal shape and yield to the intermediate mass values where MC samples are not available. Small effects of signal-background interference on the mass position, as discussed in Ref. [62], have not been taken into account.

Table 1 summarises the number of events observed in the data and the expected number of signal events for each of the 14 categories. The breakdown of expected signal events from the different production processes is also detailed. The total efficiency for the signal selection is expected to be 37.5% for a Higgs boson with $m_H = 125$ GeV.

Table 2 gives the mass resolution and signal over background ratio in a mass window around $m_H = 126.5$ GeV containing 90% of the expected signal events for the 14 categories of the 8 TeV data analysis. The resolution of the reconstructed diphoton mass (σ_{CB}) is dominated by the photon energy resolution. It is 1.77 GeV for the inclusive analysis, with values varying from 1.40 GeV for the unconverted central high p_{Tt} to 2.52 GeV for the converted transition categories defined in Section 4.

Table 1: Number of events in the data (N_D) and expected number of SM Higgs signal events (N_S) for $m_H = 126.5$ GeV from the $H \to \gamma\gamma$ analysis, for each category in the mass range 100-160 GeV at $\sqrt{s} = 8$ TeV. Numbers for the 7 TeV analysis can be found in Ref. [4]. The statistical uncertainties in N_S are less than 1%. The fractions of expected signal events from the $gg \to H$, VBF, WH, ZH, ttH processes are detailed.

$\sqrt{s}$	8 TeV						
Category	N_D	N_S	$gg \to H$ [%]	VBF [%]	WH [%]	ZH [%]	ttH [%]
Unconv. central, low p_{Tt}	10900	51.8	93.7	4.0	1.4	0.8	0.2
Unconv. central, high p_{Tt}	553	7.9	79.3	12.6	4.1	2.5	1.4
Unconv. rest, low p_{Tt}	41236	107.9	93.2	4.0	1.6	1.0	0.1
Unconv. rest, high p_{Tt}	2558	16.0	78.1	13.3	4.7	2.8	1.1
Conv. central, low p_{Tt}	7109	33.1	93.6	4.0	1.3	0.9	0.2
Conv. central, high p_{Tt}	363	5.1	78.9	12.6	4.3	2.7	1.5
Conv. rest, low p_{Tt}	38156	97.8	93.2	4.1	1.6	1.0	0.1
Conv. rest, high p_{Tt}	2360	14.4	77.7	13.0	5.2	3.0	1.1
Conv. transition	14864	40.1	90.7	5.5	2.2	1.3	0.2
Loose high-mass two-jet	276	5.3	45.0	54.1	0.5	0.3	0.1
Tight high-mass two-jet	136	8.1	23.8	76.0	0.1	0.1	0.0
Low-mass two-jet	210	3.3	48.1	3.0	29.7	17.2	1.9
$E_{\mathrm{T}}^{\mathrm{miss}}$ significance	49	1.3	4.1	0.5	35.7	47.6	12.1
One-lepton	123	2.9	2.2	0.6	63.2	15.4	18.6
All categories (inclusive)	118893	395.0	88.0	7.3	2.7	1.5	0.5

Table 2: Signal mass resolution (σ_{CB}), number of observed events, number of expected signal events (N_S), number of expected background events (N_B) and signal to background ratio (N_S/N_B) in a mass window around m_H = 126.5 GeV containing 90% of the expected signal for each of the 14 categories of the 8 TeV data analysis. The numbers of background events are obtained from the background + signal fit to the $m_{\gamma\gamma}$ data distribution.

$\sqrt{s}$	8 TeV				
Category	σ_{CB}(GeV)	Observed	N_S	N_B	N_S/N_B
Unconv. central, low p_{Tt}	1.50	911	46.6	881	0.05
Unconv. central, high p_{Tt}	1.40	49	7.1	44	0.16
Unconv. rest, low p_{Tt}	1.74	4611	97.1	4347	0.02
Unconv. rest, high p_{Tt}	1.69	292	14.4	247	0.06
Conv. central, low p_{Tt}	1.68	722	29.8	687	0.04
Conv. central, high p_{Tt}	1.54	39	4.6	31	0.15
Conv. rest, low p_{Tt}	2.01	4865	88.0	4657	0.02
Conv. rest, high p_{Tt}	1.87	276	12.9	266	0.05
Conv. transition	2.52	2554	36.1	2499	0.01
Loose High-mass two-jet	1.71	40	4.8	28	0.17
Tight High-mass two-jet	1.64	24	7.3	13	0.57
Low-mass two-jet	1.62	21	3.0	21	0.14
$E_{\mathrm{T}}^{\mathrm{miss}}$ significance	1.74	8	1.1	4	0.24
One-lepton	1.75	19	2.6	12	0.20
Inclusive	1.77	14025	355.5	13280	0.03

5.2 Background modelling

The invariant mass distribution of the background in each category is parameterised with analytic functions. The parameters of these analytic functions are determined from fits to the data in the 100-160 GeV diphoton invariant mass range. The choice of the functional form for the categories is based on studies on MC samples where the γ-γ (Sherpa [63], Diphox [64], MadGraph [65]), γ-jets (Sherpa), jet-jet (Pythia [66]), and Drell-Yan (Pythia) components are combined according to the fractions determined from data-driven measurements [13]. In the Sherpa and Pythia samples, detector effects are taken into account, including photon identification efficiency, photon energy resolution, jets misidentified as photons and the fraction of converted photons in the different detector regions. In the Diphox samples, photon identification efficiency is taken into account.

The choice of the function follows the method described in Ref. [6]. Depending on the category, it is either a fourth-order Bernstein polynomial, the exponential of a second-order polynomial, or a single exponential. For the inclusive data sample a fourth-order Bernstein polynomial is used. The systematic uncertainty on the background model (Table 4) is defined as the largest absolute signal component fitted anywhere in the full mass range studied [110-150] GeV with the background samples described above. Because of the small number of events in the $E_{\mathrm{T}}^{\mathrm{miss}}$ significance category, the background uncertainty is estimated with the inclusive $m_{\gamma\gamma}$ spectrum using the ratio of yields between the inclusive and the $E_{\mathrm{T}}^{\mathrm{miss}}$ significance selections.

The inclusive invariant mass distribution of the diphoton candidates for the combined $\sqrt{s}$ = 7 TeV and $\sqrt{s}$ = 8 TeV data sample is shown in Figure 3 with overlaid signal-plus-background fit.

The excess of events around m_H= 126.5 GeV is discussed in detail in Section 7.

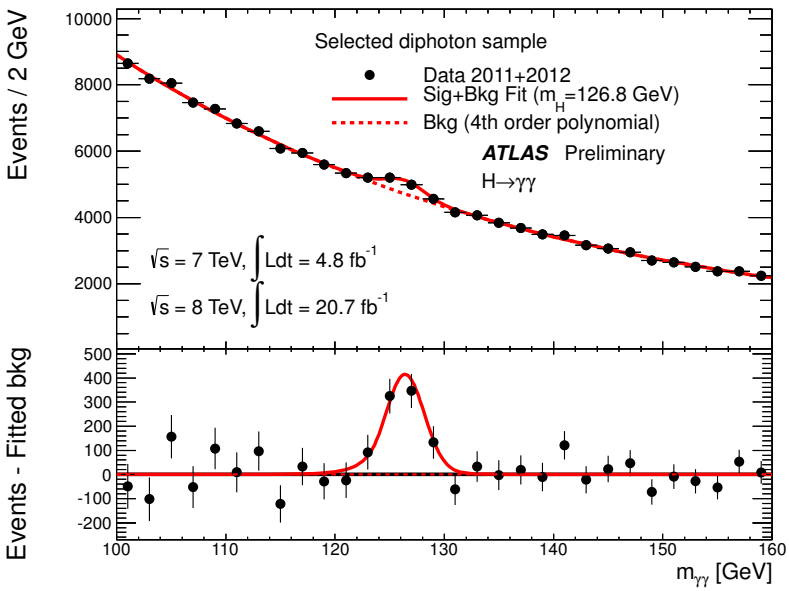

Figure 3: Invariant mass distribution of diphoton candidates for the combined $\sqrt{s}$ = 7 TeV and $\sqrt{s}$ = 8 TeV data samples. The result of a fit to the data of the sum of a signal component fixed to m_H = 126.8 GeV and a background component described by a fourth-order Bernstein polynomial is superimposed. The bottom inset displays the residuals of the data with respect to the fitted background component.

6 Systematic uncertainties

Most of the systematic uncertainties of this analysis are discussed in Ref. [6] and [13]. These will be only briefly described and updated here, while new systematic uncertainties arising from the introduction of additional categories will be adressed in more detail. All uncertainties are treated as fully correlated between 7 and 8 TeV data except that on the luminosity. The uncertainties can affect the signal yield, the signal resolution, the migration of events between categories and the mass measurement.

6.1 Uncertainties on the signal yield

The systematic uncertainties affecting the signal yield are the following:

- The uncertainty on the integrated luminosity is ±3.6% for the 8 TeV data. It is obtained, following the same methodology as that detailed in Ref. [67], from a preliminary calibration of the luminosity scale derived from beam-separation scans performed in April 2012. For the 7 TeV data this uncertainty has been updated to 1.8%.

- The uncertainty on the trigger efficiency is 0.5% per event;

- The uncertainty on the photon identification efficiency for the 8 TeV analysis has decreased with respect to Ref. [6]. It is based on the comparison of the efficiency obtained using MC and the combination of data-driven measurements: extrapolation from $Z \to ee$ events, a method using an inclusive photon sample and relying on a sideband technique, and radiative photons Z→ $\ell\ell\gamma$

studies based on more than 10 fb^{-1} of data. It also benefits from a better treatment of the multi-photon correlations. The resulting uncertainty on the event yield is 2.4%;

- The isolation cut efficiency, estimated by comparing data and MC for $Z \to ee$ events, introduces an uncertainty of 1%;
- The uncertainty on the photon energy scale leads to an uncertainty on the signal yield amounting to 0.25%;
- The theoretical uncertainties on the Higgs boson production, including PDF, missing higher order perturbative QCD corrections, and branching ratio, are unchanged from [13]. The followed prescriptions are detailed in [57, 58, 68];
- The theoretical uncertainty on the ggF+2 jet cross section prediction affects the high-mass two-jet category in particular. The uncertainty due to missing higher orders has been determined using a new approach [69], based on the MCFM [70] calculation. The new procedure uses an infrared sensitive variable, $\Delta\Phi_{\gamma\gamma;jj}$, and the change of its distribution after the VBF selection to estimate the uncertainty. The uncertainty determined in this way was compared to the estimate using MCFM and was found to be in good agreement. These uncertainties are 48% (28%) in the tight (loose) high-mass two-jet categories. For the low-mass two-jet category MCFM based uncertainties are used, resulting in a 30% uncertainty.

These uncertainties are summarized in Table 5. The uncertainty on the background modelling is addressed in Section 5.2.

6.2 Uncertainties on the signal resolution

The uncertainties affecting the mass resolution are:

- The calorimeter energy resolution uncertainty together with the uncertainty arising from the extrapolation from the electron to photon response, evaluated separately for each category, is found to be between 14 and 23% depending on the category. This uncertainty is larger than in the previous analysis [6] because it now takes into account additional differences observed between $Z \to ee$ data and MC events, as described in Section 5.1.
- Pile-up mis-modelling gives a $\pm 1.5\%$ uncertainty;
- The uncertainty associated with the primary vertex selection, at the level of 0.2%, is considered negligible.

6.3 Migration uncertainties

The following sources produce uncertainties in the fraction of events being classified in different categories (migration). They are summarized in Table 6.

- The material mis-modelling impact is at the level of -4% for unconverted photons categories and +3.5% for converted photons categories;
- The uncertainty in the population of the p_{Tt} categories due to the modelling of the Higgs boson kinematic properties is estimated by varying scales and PDFs used by `HqT2` [58, 71] and has a 1.3% impact on the low-p_{Tt} categories, 10.2% on the high-p_{Tt} categories, 10.4% (8.5%) on the tight (loose) high-mass two-jet categories, 12.5% on the low-mass two-jet category, 2.0% on the $E_{\mathrm{T}}^{\mathrm{miss}}$ category, and 4.0% on the one-lepton category;

- The uncertainties on the jet energy scale induce an effect of up to 11.8% (10.7%) for the tight (loose) high-mass two-jet category, a 6.7% effect on the low-mass two-jet category and up to 0.7% for the other categories. The impact of the uncertainty on the jet energy resolution is found to be up to 3.8% (3.4%) on the tight (loose) high-mass two-jet category, 3.4% on the low-mass two-jet category, and up to 0.9% on the other categories;

- The uncertainty due to the modelling of the underlying event is estimated by comparing simulations with and without multi-parton interaction (MPI). The AU2-CT10 [72] tune is used for the default results, while samples without MPI are used for systematics studies. For the tight high-mass two-jet category, 8.8% uncertainty is assigned to ggF, VH and ttH and 2.0% to VBF. For the loose high-mass two-jet category, these uncertainties are 12.8% and 3.3% respectively. For the low-mass two-jet category, the uncertainty is found to be 12% for the ggF, VH and ttH processes and 3.9% for VBF;

- A systematic uncertainty is assigned to the modelling of the two-jet variables, in particular $\Delta\phi_{\gamma\gamma;jj}$, in Powheg for the ggF process, which is described with NLO QCD accuracy. Powheg distributions are compared to those from LO Sherpa with matrix element matching for up to three partons in the final state, and reweighted. The resulting systematic uncertainties are 12.1% (8.5%) in the tight (loose) high-mass two-jet categories respectively;

- The systematic uncertainty coming from the modelling of the η^* variable (defined in Section 4.3) in Powheg for the ggF process is estimated by reweighting the jet distribution at the MC generator level to the MCFM distribution. The corresponding uncertainty for the tight (loose) high-mass two-jet category is 7.6% (6.2%);

- A systematic uncertainty is associated to the cut on the jet vertex fraction JVF, amounting to 0.3(1.2)% in the loose high-mass two-jet category for ggF (VBF), and 2.3(2.4)% in the low-mass two-jet category for ggF (VBF);

- The electron reconstruction and identification efficiency ($< 1\%$), electron energy scale and resolution ($< 1\%$); the muon reconstruction efficiency, tracker resolution ($< 1\%$) and muon spectrometer resolution (negligible). These uncertainties are only applied to the WH, ZH and ttH processes;

- $E_{\mathrm{T}}^{\mathrm{miss}}$ uncertainties are assessed by shifting the transverse energy of each of the input objects (photons, electrons, jets, soft terms) up and down by the uncertainties on their resolution and scale. The resulting uncertainty on the $E_{\mathrm{T}}^{\mathrm{miss}}$ category is 66.4% for gluon fusion production, 30.7% for VBF production and 1.2% for the associated production. The largest contributions come from the soft terms. The jet related terms are correlated to the jet energy scale and jet energy resolution uncertainties.

6.4 Mass uncertainties

The main sources of uncertainties on the mass measurement are evaluated separately for the different categories. They arise from the extrapolation of the photon energy scale from the $Z \to ee$ electron energy scale (0.3%), the material modelling (0.3%) and the presampler energy scale (0.1%). These systematic uncertainties amount to a total of 0.45% (0.6 GeV).

Dedicated cross checks have been performed on the mass measurement and additional systematic uncertainties have been quantified in Ref. [6]. They are not treated as category-dependent. With respect to this previous result, the uncertainty of 0.15% coming from varying the signal resolution within its uncertainties was removed after more checks. These additional uncertainties on the mass measurement amount to a total of 0.32% (0.4 GeV).

The total systematic uncertainty on the mass measurement is estimated to be 0.55% (0.7 GeV).

It has been checked that the mass measurements in subsets of the data, namely in the different categories of photon p_{T} and η, or events with different numbers of primary vertices, give consistent results within the statistical errors.

7 Results

7.1 Statistical procedure

The data are interpreted following the statistical procedure summarized in Ref. [73]. The signal strength parameter μ, defined as a scale factor of the number of signal events expected from the SM Higgs boson hypothesis, is the parameter of interest. A profile likelihood ratio based test statistic $\lambda(\mu)$ is used to test different hypothesised values of μ. The background-only hypothesis is tested with $\lambda(0)$ and a signal plus background hypothesis is tested with $\lambda(\mu)$. A likelihood function, describing the probability distribution function of $m_{\gamma\gamma}$ under a μ-times-signal plus background hypothesis as well as the systematic uncertainties, is used to build $\lambda(\mu)$. The likelihood function from the analysis of the 8 TeV data is combined with the likelihood function from the analysis of the 7 TeV data.

The statistical tests are carried out at a series of values of m_H from 110 GeV to 150 GeV in which the step size is 0.5 GeV.

The local p_0 value, the probability of the background fluctuating beyond the observation in the data at a particular m_H, is calculated to quantify the significance of an excess. It is also converted to the number of standard deviations from the background-only hypothesis and referred to as the local significance.

7.2 Signal significance

The observed local p_0 values, as well as the expected p_0 values corresponding to a SM Higgs boson signal plus background hypothesis, are shown in Figure 4 as a function of m_H. The largest local significance in the combination of 7 TeV and 8 TeV data is found to be 7.4 σ at $m_H = 126.5$ GeV, where the expected significance is 4.1 σ. The largest observed (expected) local significance for the inclusive analysis is 6.1(2.9) σ.

7.3 Mass measurement and signal strength

7.3.1 Mass measurement

The parameter of interest in the test statistic is changed to m_H in order to estimate the mass of the observed new particle, and the signal strength parameter μ is treated as a free parameter in the fits. The best-fit m_H value is found to be 126.8 GeV, and its statistical and systematic uncertainties are ±0.2 GeV and ±0.7 GeV, respectively. With this larger data sample, the value of the measured mass increases by 200 MeV compared to Ref [6]. The dominant contribution to the systematic uncertainty comes from the uncertainties on the photon energy scale.

7.3.2 Signal strength

The best-fit values of the signal strength μ and m_H are shown in Figure 5. At the best-fit value $m_H = 126.8$ GeV, μ is found to be $1.65^{+0.34}_{-0.30}$. The μ uncertainty of $^{+0.34}_{-0.30}$ is further broken down to $^{+0.24}_{-0.24}$(stat) and $^{+0.25}_{-0.18}$(syst). The systematic uncertainty includes the signal yield, signal resolution and migration uncertainties and the uncertainties on the inclusive Higgs boson production cross section and decay branching ratio.

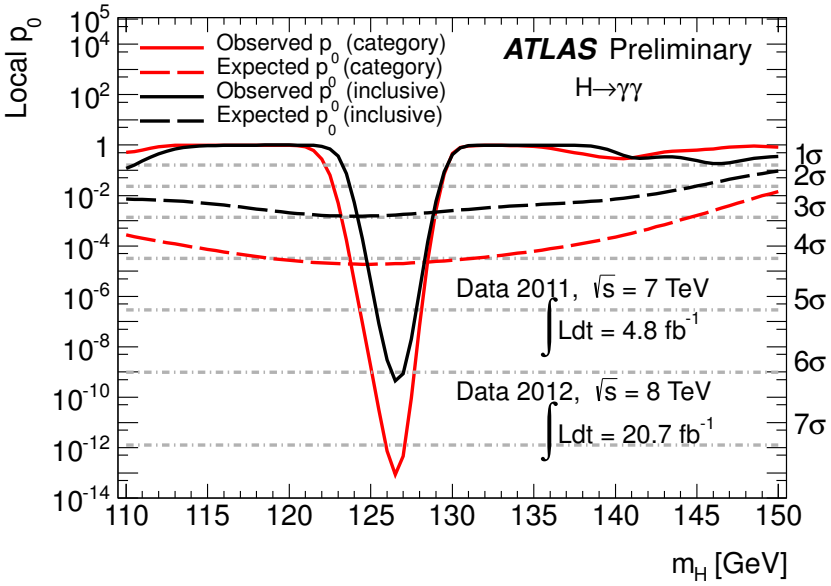

Figure 4: The observed local p_0 value as a function of m_H for the combination of $\sqrt{s}$ = 7 TeV and $\sqrt{s}$ = 8 TeV data for the inclusive case (black) and for the analysis using categories (red). The expected local p_0 under the SM Higgs boson signal plus background hypothesis is shown by the dashed curves.

The compatibility in the signal strength parameter between the data and the SM Higgs boson signal plus background hypothesis is estimated with the test statistic $\lambda(\mu)$ with $\mu = 1$ [4], and is found to be at the 2.3 σ level.

The results reported above are extracted from a fit in which the mass resolution uncertainty, which is ~20%, is treated as a nuisance parameter with a Gaussian constraint. As a check, the fit was repeated with no constraint on the mass resolution parameter, giving $\mu = 1.49 \pm 0.33$ (1.8 σ compatibility with the SM Higgs boson signal hypothesis). This fit prefers a narrower mass resolution than the nominal one by 1.8 σ, which is better than the resolution corresponding to a perfectly uniform calorimeter. Dedicated studies revealed no indication that the systematic uncertainty on the resolution is underestimated; the large pull in this test fit can also be a statistical effect arising from background fluctuations.

The effects of systematic uncertainties, in particular the photon energy scale, on the measurement of mass and signal strength are shown in Figure 5.

7.4 Couplings and production modes

As discussed in Section 4, several categories targeting different production modes have been introduced. Two of them (loose and tight high-mass two-jet) are enriched in VBF events, and three of them (low-mass two-jet, $E_{\mathrm{T}}^{\mathrm{miss}}$ significance and one-lepton) are enriched in VH events. Such an analysis provides constraints on the signal strength of individual production modes.

First, the observed and expected local p_0^{VBF} value corresponding to a SM Higgs boson signal produced in VBF plus background hypothesis is computed as a function of m_H. The ggF, WH, ZH and ttH processes are considered as background here and their respective signal strengths are treated as nuisance parameters. The resulting local p_0^{VBF} value from the combination of 7 TeV and 8 TeV data is shown in Figure 6. The largest local significance is found to be 2.9 σ at m_H = 123.5 GeV where the expected

[4] The unconditional maximum likelihood estimator μ is restricted to be equal to or larger than 1 in $\lambda(1)$.

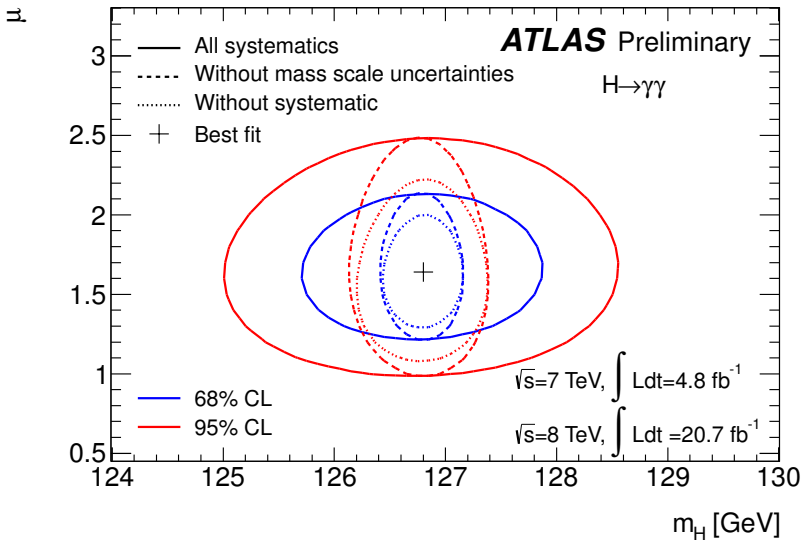

Figure 5: The best-fit values of m_H and μ, and their 68% (blue) and 95% (red) CL contours. Results when photon energy scale systematic uncertainties are removed (dashed), and results when all systematic uncertainties are removed (dotted), are also shown.

significance is 1.3 σ. The expected (observed) significances at $m_H = 126.8$ GeV are 1.3 σ (2.0 σ) respectively.

In a second step, signal strength parameters for different Higgs boson production modes are introduced to characterise their contributions to the observed excess. To further enhance the sensitivity, the ggF and ttH processes are grouped together to share the same signal strength parameter, $\mu_{ggF+ttH}$, as they both involve the coupling between a Higgs boson and top quarks. Similarly, the VBF and VH processes are grouped together to share the same signal strength parameter μ_{VBF+VH}. The fitted $\mu_{\mathrm{ggF+ttH}}$ and $\mu_{\mathrm{VBF+VH}}$ are muliplied by a common scale factor B/B_{SM}, where B is the branching ratio for $H \to \gamma\gamma$ and B_{SM} is the branching ratio for $H \to \gamma\gamma$ predicted by the SM. The simultaneously fitted values of $\mu_{\mathrm{ggF+ttH}} \times B/B_{\mathrm{SM}}$ and $\mu_{\mathrm{VBF+VH}} \times B/B_{\mathrm{SM}}$ in data are presented in Figure 7, where the 68% and 95% CL contours are also shown. A simultaneous fit is also performed to determine the signal strengths of $\mu_{\mathrm{ggF+ttH}} \times B/B_{\mathrm{SM}}$, $\mu_{\mathrm{VBF}} \times B/B_{\mathrm{SM}}$, and $\mu_{\mathrm{VH}} \times B/B_{\mathrm{SM}}$, where the VBF and VH production modes are separated, and the best-fit values are:

- $\mu_{\mathrm{ggF+ttH}} \times B/B_{\mathrm{SM}} = 1.6^{+0.3}_{-0.3}(\mathrm{stat})^{+0.3}_{-0.2}(\mathrm{syst})$;
- $\mu_{\mathrm{VBF}} \times B/B_{\mathrm{SM}} = 1.7^{+0.8}_{-0.8}(\mathrm{stat})^{+0.5}_{-0.4}(\mathrm{syst})$. The total expected uncertainty is improved by 32% with respect to the analysis described in Ref. [6] for the same integrated luminosity;
- $\mu_{\mathrm{VH}} \times B/B_{\mathrm{SM}} = 1.8^{+1.5}_{-1.3}(\mathrm{stat})^{+0.3}_{-0.3}(\mathrm{syst})$. The total expected uncertainty is improved by 27% with respect to the analysis described in Ref. [6] for the same integrated luminosity.

These results are also shown in Figure 8.

7.5 Fiducial cross section

The cross section in the fiducial region, σ_{fid}, for the production of the observed particle at a mass of 126.8 GeV was measured with the $\sqrt{s} = 8$ TeV data corresponding to an integrated luminosity of 20.7 fb^{-1}. The

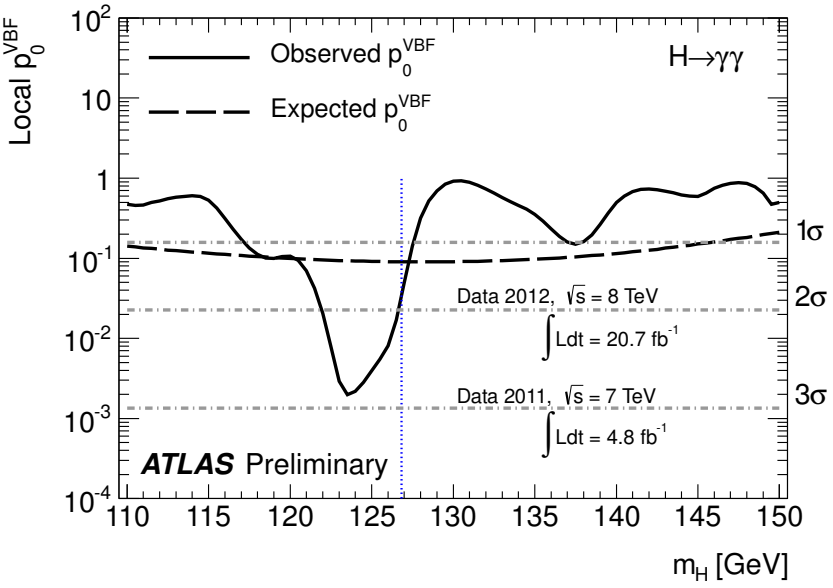

Figure 6: The observed local p_0^{VBF} value for VBF $H \rightarrow \gamma\gamma$ production as a function of m_H for the combination of $\sqrt{s} = 7$ TeV and $\sqrt{s} = 8$ TeV data (solid black). The corresponding expected local p_0^{VBF} value for the SM Higgs boson signal plus background hypothesis are shown by the dashed curve. A vertical line is drawn at the best-fit mass $m_H = 126.8$ GeV.

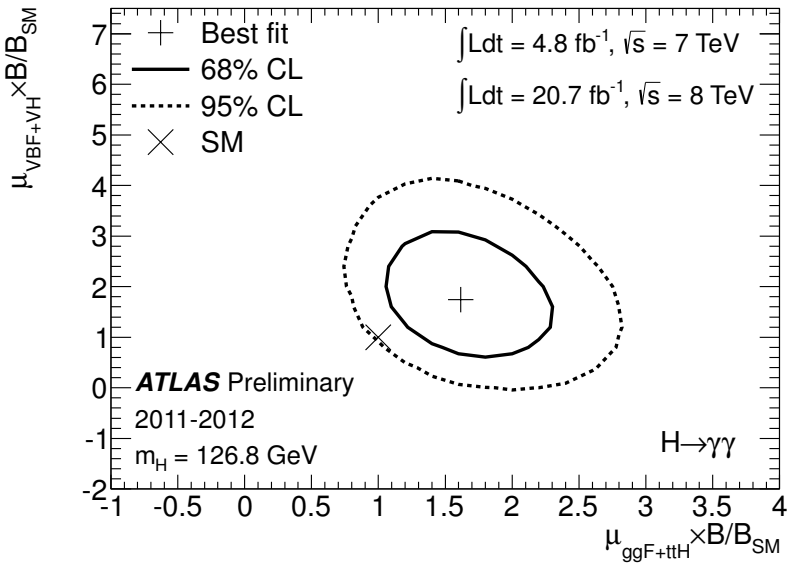

Figure 7: The best-fit values (+) of $\mu_{ggF+ttH} \times B/B_{SM}$ and $\mu_{VBF+VH} \times B/B_{SM}$ from a simultaneous fit to the data and their 68% (solid) and 95% (dashed) CL contours. The expectation for a SM Higgs boson is also shown (×).

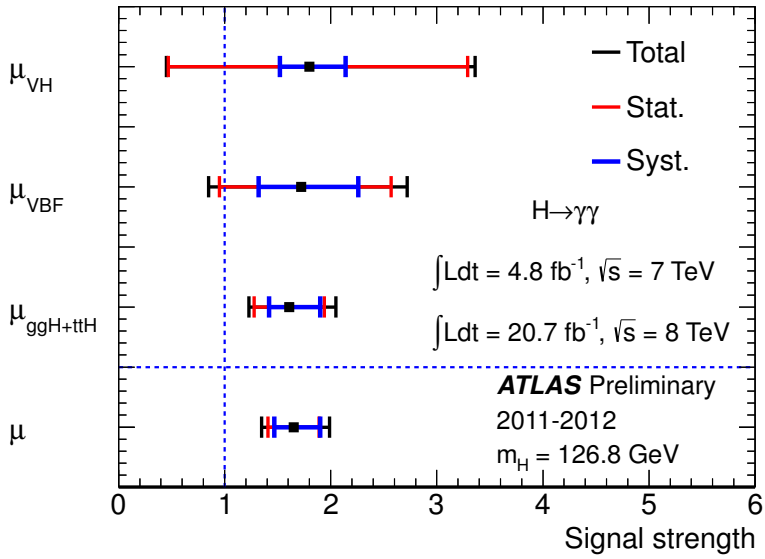

Figure 8: Measured signal strengths $\mu_{ggF+ttH}$, μ_{VBF} and μ_{VH} for the different $H \to \gamma\gamma$ production modes, as well as overall strength μ.

analysis without categories (inclusive analysis) was used since it is less model dependent than the analysis using categories. Since extrapolation to the full phase space is not considered, these cross sections are largely unaffected by theoretical uncertainties. The fiducial region is defined, for isolated photons, by the photon pseudorapidity ($|\eta| < 2.37$) and transverse energies ($E_T^{\gamma 1} > 40$ GeV and $E_T^{\gamma 2} > 30$ GeV).

This fiducial cross section times the branching ratio to the two photons decay mode is computed as:

$$\sigma_{\text{fid}} \times \text{BR} = \frac{N^{\text{signal}}}{C_H \times L_{\text{int}}} \tag{1}$$

where:

- N^{signal} is the number of signal events extracted from a signal-plus-background fit to the inclusive $m_{\gamma\gamma}$ distribution;
- C_H is a correction factor for detector effects (including efficiencies for triggering, reconstructing, and identifying the photons, photon isolation) for photons inside the acceptance;
- L_{int} is the integrated luminosity.

The number of signal events extracted from the signal-plus-background fit is 748 ± 139 (stat). A systematic uncertainty of 11.2% on this number is due to the uncertainties on the mass resolution and background modelling. These uncertainties are treated in the fit as nuisance parameters with Gaussian constraints.

The C_H factor is computed from the Higgs boson Monte Carlo samples and is defined as the ratio between the total number of generated events passing the final selection requirements after reconstruction and the total number of generated events within the fiducial acceptance. These factors are determined for each production mode and differ only by a few percent, except for the ttH process for which the difference is up to 30%. This difference is due to the additional hadronic activity which affects the photon isolation cut efficiency. The global C_H factor is computed from the cross section weighted contributions from the

different processes and is equal to 0.643. It is dominated by the contribution of the gluon fusion process, thus valid for isolated photons.

The following sources of uncertainty on the C_H factor have been considered (see Section 6.1): photon identification (2.4%), energy scale (0.25%), isolation (1%) and trigger (0.5%). The influence of the modelling of the Higgs boson transverse momentum was checked with `HqT2` [71] and found to be negligible. The effects of the factorisation and renormalisation scales, PDF and underlying event were also checked and found to be below 0.2%; they are thus neglected. The C_H factor depends weakly on the mass. It is computed for a mass of 125 GeV while the cross section is computed for 126.8 GeV. The difference, of the order of 0.1%, is neglected. The total uncertainty on the C_H factor is therefore 2.7%, and the total systematic uncertainty on the fiducial cross section is 11.5%.

The measured fiducial cross section times the branching ratio to the two photons decay mode is:

$$\sigma_{\text{fid}} \times BR = 56.2 \pm 10.5(\text{stat}) \pm 6.5(\text{syst}) \pm 2.0(\text{lumi}) \text{ fb}$$

This result is compatible with the SM Higgs signal prediction measured using the same sample.

8 Conclusions

Measurements of the properties of the new observed boson were performed in the $H \to \gamma\gamma$ channel with the ATLAS experiment at the LHC using 20.7 fb^{-1} of pp collision data recorded between April and December 2012 at a centre-of-mass energy of 8 TeV. These results were combined with those obtained using 4.8 fb^{-1} of data recorded in 2011 at 7 TeV.

- An excess of events is observed with a local significance of 7.4 σ,
- The measured mass of the boson is $126.8 \pm 0.2(\text{stat}) \pm 0.7(\text{syst})$ GeV,
- The signal strength is $1.65^{+0.24}_{-0.24}(\text{stat})^{+0.25}_{-0.18}(\text{syst})$ times the SM expectation for $m_H = 126.8$ GeV which corresponds to a 2.3 σ deviation from the SM prediction,
- An excess with local significance 2.0 σ is observed for the VBF production mode alone for a mass of 126.8 GeV,
- The signal strengths for the different production modes are:

$$\mu_{\text{ggF+ttH}} \times B/B_{\text{SM}} = 1.6^{+0.3}_{-0.3}(\text{stat})^{+0.3}_{-0.2}(\text{syst})$$
$$\mu_{\text{VBF}} \times B/B_{\text{SM}} = 1.7^{+0.8}_{-0.8}(\text{stat})^{+0.5}_{-0.4}(\text{syst})$$
$$\mu_{\text{VH}} \times B/B_{\text{SM}} = 1.8^{+1.5}_{-1.3}(\text{stat})^{+0.3}_{-0.3}(\text{syst})$$

The fiducial cross section times branching ratio to the two photon decay mode, defined for the kinematic range $E_T^{\gamma 1} > 40$ GeV, $E_T^{\gamma 2} > 30$ GeV and $|\eta^{\gamma}| < 2.37$, and measured using 20.7 fb^{-1} of data at $\sqrt{s} = 8$ TeV, is $56.2 \pm 10.5(\text{stat}) \pm 6.5(\text{syst}) \pm 2.0(\text{lumi})$ fb.

References

[1] F. Englert and R. Brout, *Broken symmetry and the mass of gauge vector mesons*, Phys. Rev. Lett. **13** (1964) 321.

[2] P. W. Higgs, *Broken symmetries and the masses of gauge bosons*, Phys. Rev. Lett. **13** (1964) 508.

[3] G. Guralnik, C. Hagen, and T. Kibble, *Global conservation laws and massless particles*, Phys. Rev. Lett. **13** (1964) 585.

[4] ATLAS Collaboration, *Observation of a new particle in the search for the Standard Model Higgs boson with the ATLAS detector at the LHC*, Phys.Lett. **B716** (2012) 1, arXiv:1207.7214 [hep-ex].

[5] CMS Collaboration, *Observation of a new boson at a mass of 125 GeV with the CMS experiment at the LHC*, Phys.Lett. **B716** (2012) 30, arXiv:1207.7235 [hep-ex].

[6] ATLAS Collaboration, *Observation and study of the Higgs boson candidate in the two photon decay channel with the ATLAS detector at the LHC*, ATLAS-CONF-2012-168 (2012).

[7] ATLAS Collaboration, *The ATLAS experiment at the CERN Large Hadron Collider*, JINST **3** (2008) S08003.

[8] ATLAS Collaboration, *Expected photon performance in the ATLAS experiment*, ATLAS-PHYS-PUB-2011-007 (2011).

[9] W. Lampl, S. Laplace, D. Lelas, P. Loch, H. Ma, S. Menke, S. Rajagopalan, D. Rousseau, S. Snyder, and G. Unal, *Calorimeter clustering algorithms: description and performance*, ATL-LARG-PUB-2008-002 (2008).

[10] ATLAS Collaboration, *Calorimeter isolation with topoclusters versus pile-up,* https://atlas.web.cern.ch/Atlas/GROUPS/PHYSICS/EGAMMA/PublicPlots/20120404/TopoIsolation/ATL-COM-PHYS-2012-362/index.html, (2012).

[11] M. Cacciari and G. P. Salam, *Pileup subtraction using jet areas*, Physics Letters B **659** (2008) 119.

[12] ATLAS Collaboration, *Electron performance measurements with the ATLAS detector using the 2010 LHC proton-proton collision data*, Eur. Phys. J. **C72** (2012) 1909, arXiv:1110.3174 [hep-ex].

[13] ATLAS Collaboration, *Observation of an excess of events in the search for the Standard Model Higgs boson in the gamma-gamma channel with the ATLAS detector*, ATLAS-CONF-2012-091 (2012).

[14] M. Cacciari, G. P. Salam, and G. Soyez, *The anti-k_t jet clustering algorithm*, JHEP **0804** (2008) 063, arXiv:0802.1189 [hep-ph].

[15] ATLAS Collaboration, *Jet energy scale and its systematic uncertainty in proton-proton collisions at $\sqrt{s}$ = 7 TeV with ATLAS 2011 data*, ATLAS-CONF-2013-004 (2013).

[16] ATLAS Collaboration, *Performance of missing transverse momentum reconstruction in ATLAS with 2011 proton-proton collisions at $\sqrt{s}$ = 7 TeV*, ATLAS-CONF-2012-101 (2012).

[17] OPAL Collaboration, *Search for anomalous production of di-lepton events with missing transverse momentum in e^+e^- collisions at $\sqrt{s}$ = 161 and 172 GeV*, Eur. Phys. J. **C4** (1998) 47.

[18] M. Vesterinen and T. R. Wyatt, *A novel technique for studying the Z boson transverse momentum distribution at hadron colliders*, Nucl. Instrum. Meth. **A602** (2009) 432.

[19] A. Hoecker, P. Speckmayer, J. Stelzer, J. Therhaag, E. von Toerne, and H. Voss, *TMVA 4 (Toolkit for multivariate data analysis with ROOT) Users Guide*. 2009.

[20] D. Rainwater, R. Szalapski, and D. Zeppenfeld, *Probing color-singlet exchange in Z + 2-jet events at the CERN LHC*, Phys. Rev. D **54** (1996) 6680.

[21] S. Alioli, P. Nason, C. Oleari, and E. Re, *NLO Higgs boson production via gluon fusion matched with shower in POWHEG*, JHEP **0904** (2009) 002, arXiv:0812.0578 [hep-ph].

[22] P. Nason and C. Oleari, *NLO Higgs boson production via vector-boson fusion matched with shower in POWHEG*, JHEP **1002** (2010) 037, arXiv:0911.5299 [hep-ph].

[23] T. Sjostrand, S. Mrenna, and P. Z. Skands, *PYTHIA 6.4 Physics and Manual*, JHEP **0605** (2006) 026, arXiv:hep-ph/0603175 [hep-ph].

[24] A. Djouadi, M. Spira, and P. Zerwas, *Production of Higgs bosons in proton colliders: QCD corrections*, Phys. Lett. **B264** (1991) 440.

[25] S. Dawson, *Radiative corrections to Higgs boson production*, Nucl. Phys. **B359** (1991) 283.

[26] M. Spira, A. Djouadi, D. Graudenz, and P. Zerwas, *Higgs boson production at the LHC*, Nucl. Phys. **B453** (1995) 17, arXiv:hep-ph/9504378 [hep-ph].

[27] R. V. Harlander and W. B. Kilgore, *Next-to-next-to-leading order Higgs production at hadron colliders*, Phys. Rev. Lett. **88** (2002) 201801, arXiv:hep-ph/0201206 [hep-ph].

[28] C. Anastasiou and K. Melnikov, *Higgs boson production at hadron colliders in NNLO QCD*, Nucl. Phys. **B646** (2002) 220, arXiv:hep-ph/0207004 [hep-ph].

[29] V. Ravindran, J. Smith, and W. L. van Neerven, *NNLO corrections to the total cross-section for Higgs boson production in hadron hadron collisions*, Nucl. Phys. **B665** (2003) 325, arXiv:hep-ph/0302135 [hep-ph].

[30] S. Catani, D. de Florian, M. Grazzini, and P. Nason, *Soft gluon resummation for Higgs boson production at hadron colliders*, JHEP **0307** (2003) 028, arXiv:hep-ph/0306211 [hep-ph].

[31] E. Bagnaschi, G. Degrassi, P. Slavich, and A. Vicini, *Higgs production via gluon fusion in the POWHEG approach in the SM and in the MSSM*, JHEP **1202** (2012) 088, arXiv:1111.2854 [hep-ph].

[32] U. Aglietti, R. Bonciani, G. Degrassi, and A. Vicini, *Two loop light fermion contribution to Higgs production and decays*, Phys. Lett. **B595** (2004) 432, arXiv:hep-ph/0404071 [hep-ph].

[33] S. Actis, G. Passarino, C. Sturm, and S. Uccirati, *NLO electroweak corrections to Higgs boson production at hadron colliders*, Phys. Lett. **B670** (2008) 12, arXiv:0809.1301 [hep-ph].

[34] D. de Florian and M. Grazzini, *Higgs production at the LHC: updated cross sections at* $\sqrt{s}$ = 8 TeV, arXiv:1206.4133 [hep-ph].

[35] C. Anastasiou, S. Buehler, F. Herzog, and A. Lazopoulos, *Inclusive Higgs boson cross-section for the LHC at 8 TeV*, JHEP **1204** (2012) 004, arXiv:1202.3638 [hep-ph].

[36] J. Baglio and A. Djouadi, *Higgs production at the lHC*, JHEP **1103** (2011) 055, arXiv:1012.0530 [hep-ph].

[37] M. Ciccolini, A. Denner, and S. Dittmaier, *Strong and electroweak corrections to the production of Higgs + 2-jets via weak interactions at the LHC*, Phys. Rev. Lett. **99** (2007) 161803, arXiv:0707.0381 [hep-ph].

[38] M. Ciccolini, A. Denner, and S. Dittmaier, *Electroweak and QCD corrections to Higgs production via vector-boson fusion at the LHC*, Phys. Rev. **D77** (2008) 013002, arXiv:0710.4749 [hep-ph].

[39] K. Arnold et al., *VBFNLO: A Parton level Monte Carlo for processes with electroweak bosons*, Comput. Phys. Commun. **180** (2009) 1661, arXiv:0811.4559 [hep-ph].

[40] P. Bolzoni, F. Maltoni, S.-O. Moch, and M. Zaro, *Higgs production via vector-boson fusion at NNLO in QCD*, Phys. Rev. Lett. **105** (2010) 011801, arXiv:1003.4451 [hep-ph].

[41] T. Han and S. Willenbrock, *QCD correction to the $pp \to WH$ and ZH total cross-sections*, Phys. Lett. **B273** (1991) 167.

[42] O. Brein, A. Djouadi, and R. Harlander, *NNLO QCD corrections to the Higgs-strahlung processes at hadron colliders*, Phys. Lett. **B579** (2004) 149, arXiv:hep-ph/0307206 [hep-ph].

[43] M. Ciccolini, S. Dittmaier, and M. Krämer, *Electroweak radiative corrections to associated WH and ZH production at hadron colliders*, Phys. Rev. **D68** (2003) 073003, arXiv:hep-ph/0306234 [hep-ph].

[44] W. Beenakker et al., *Higgs radiation off top quarks at the Tevatron and the LHC*, Phys. Rev. Lett. **87** (2001) 201805, arXiv:hep-ph/0107081 [hep-ph].

[45] W. Beenakker et al., *NLO QCD corrections to $t\bar{t}H$ production in hadron collisions*, Nucl. Phys. **B653** (2003) 151, arXiv:hep-ph/0211352 [hep-ph].

[46] S. Dawson, L. Orr, L. Reina, and D. Wackeroth, *Next-to-leading order QCD corrections to $pp \to t\bar{t}h$ at the CERN Large Hadron Collider*, Phys. Rev. **D67** (2003) 071503, arXiv:hep-ph/0211438 [hep-ph].

[47] S. Dawson, C. Jackson, L. Orr, L. Reina, and D. Wackeroth, *Associated Higgs production with top quarks at the large hadron collider: NLO QCD corrections*, Phys. Rev. **D68** (2003) 034022, arXiv:hep-ph/0305087 [hep-ph].

[48] Lance Dixon, M. Stewart Siu, *Resonance-continuum interference in the di-photon Higgs signal at the LHC*, Phys. Rev. Lett. **90** (2003) 252001.

[49] M. Botje et al., *The PDF4LHC working group interim recommendations*, arXiv:1101.0538 [hep-ph].

[50] H.-L. Lai, M. Guzzi, J. Huston, Z. Li, P. M. Nadolsky, et al., *New parton distributions for collider physics*, Phys. Rev. **D82** (2010) 074024, arXiv:1007.2241 [hep-ph].

[51] A. Martin, W. Stirling, R. Thorne, and G. Watt, *Parton distributions for the LHC*, Eur. Phys. J. **C63** (2009) 189, arXiv:0901.0002 [hep-ph].

[52] R. D. Ball, V. Bertone, F. Cerutti, L. Del Debbio, S. Forte, et al., *Impact of heavy quark masses on parton distributions and LHC phenomenology*, Nucl. Phys. **B849** (2011) 296, arXiv:1101.1300 [hep-ph].

[53] A. Djouadi, J. Kalinowski, and M. Spira, *HDECAY: A Program for Higgs boson decays in the Standard Model and its supersymmetric extension*, Comput. Phys. Commun. **108** (1998) 56, arXiv:hep-ph/9704448 [hep-ph].

[54] A. Bredenstein, A. Denner, S. Dittmaier, and M. Weber, *Precise predictions for the Higgs-boson decay $H \to WW/ZZ \to 4$ leptons*, Phys. Rev. **D74** (2006) 013004, arXiv:hep-ph/0604011 [hep-ph].

[55] S. Actis, G. Passarino, C. Sturm, and S. Uccirati, *NNLO computational techniques: The cases $H \to \gamma\gamma$ and $H \to gg$*, Nucl. Phys. **B811** (2009) 182, arXiv:0809.3667 [hep-ph].

[56] A. Denner, S. Heinemeyer, I. Puljak, D. Rebuzzi, and M. Spira, *Standard Model Higgs-boson branching ratios with uncertainties*, Eur. Phys. J. **C71** (2011) 1753, arXiv:1107.5909 [hep-ph].

[57] LHC Higgs Cross Section Working Group, S. Dittmaier, C. Mariotti, G. Passarino, and R. Tanaka (Eds.), *Handbook of LHC Higgs Cross Sections: 1. Inclusive Observables*, CERN-2011-002 (CERN, Geneva, 2011), arXiv:1101.0593 [hep-ph].

[58] LHC Higgs Cross Section Working Group, S. Dittmaier, C. Mariotti, G. Passarino, and R. Tanaka (Eds.), *Handbook of LHC Higgs Cross Sections: 2. Differential Distributions*, CERN-2012-002 (CERN, Geneva, 2012), arXiv:1201.3084 [hep-ph].

[59] ATLAS Collaboration, *The ATLAS simulation infrastructure*, Eur. Phys. J. **C70** (2010) 823.

[60] GEANT4 Collaboration, S. Agostinelli et al., *GEANT4: A simulation toolkit*, Nucl. Instrum. Meth. **A506** (2003) 250.

[61] J. Gaiser, *Charmonium spectroscopy from radiative decays of the J/ψ and ψ'*. PhD thesis, 1982. SLAC-0255.

[62] S. P. Martin, *Shift in the LHC Higgs diphoton mass peak from interference with background*, Phys.Rev. **D86** (2012) 073016, arXiv:1208.1533 [hep-ph].

[63] T. Gleisberg, S. Hoeche, F. Krauss, M. Schonherr, S. Schumann, et al., *Event generation with SHERPA 1.1*, JHEP **0902** (2009) 007, arXiv:0811.4622 [hep-ph].

[64] T. Binoth, J. Guillet, E. Pilon, and M. Werlen, *A full next-to-leading order study of direct photon pair production in hadronic collisions*, Eur. Phys. J **C16** (2000) 311.

[65] J. Alwall, M. Herquet, F. Maltoni, O. Mattelaer, and T. Stelzer, *MadGraph 5 : Going Beyond*, JHEP **1106** (2011) 128, arXiv:1106.0522 [hep-ph].

[66] T. Sjostrand, P. Eden, C. Friberg, L. Lonnblad, G. Miu, et al., *High-energy physics event generation with PYTHIA 6.1*, Comput.Phys.Commun. **135** (2001) 238, arXiv:hep-ph/0010017 [hep-ph].

[67] ATLAS Collaboration, *Improved luminosity determination in pp collisions at $\sqrt{s} = 7$ TeV using the ATLAS detector at the LHC*, arXiv:1302.4393 [hep-ex].

[68] ATLAS Collaboration and CMS Collaboration, *Procedure for the LHC Higgs boson search combination in Summer 2011*, ATLAS-PHYS-PUB-2011-011, CMS NOTE-2011/005 (2011).

[69] S. Gangal and F. J. Tackmann, *NLO Uncertainties in Higgs + 2 jets from Gluon Fusion*, arXiv:1302.5437 [hep-ph].

[70] J. M. Campbell and R. Ellis, *MCFM for the Tevatron and the LHC*, Nucl.Phys.Proc.Suppl. **205-206** (2010) 10–15, arXiv:1007.3492 [hep-ph].

[71] D. de Florian, G. Ferrera, M. Grazzini, and D. Tommasini, *Transverse-momentum resummation: Higgs boson production at the Tevatron and the LHC*, JHEP **1111** (2011) 064, arXiv:1109.2109 [hep-ph].

[72] ATLAS Collaboration, *Summary of ATLAS Pythia 8 tunes*, ATL-PHYS-PUB-2012-003 (2012).

[73] Glen Cowan, Kyle Cranmer, Eilam Gross, Ofer Vitells, *Asymptotic formulae for likelihood-based tests of new physics*, Eur.Phys.J.C **71** (2011) 1554.

Auxiliary Plots and Tables

Table 3: Cross sections for the Standard Model Higgs boson production with m_H = 126.5 GeV at $\sqrt{s}$ = 8 TeV [57, 58]. The branching ratio to the two photons decay mode is $2.28 \cdot 10^{-3}$ at m_H = 126.5 GeV. Gluon fusion and vector boson fusion cross sections are computed in the complex pole scheme at NNLL+NNLO QCD and NLO EW [58]. Associated production cross section are computed with zero-width-approximation at NNLO QCD and NLO EW. The ttH process cross section is computed with zero-width-approximation at NLO QCD. QCD scale (±Scale) and the PDF+α_s uncertainties are treated as non-correlated [68].

Process	Cross section (pb)	+Scale %	-Scale %	+(PDF+α_s)%	-(PDF+α_s)%
ggF	19.07	+7.2	-7.8	+7.5	-6.9
VBF	1.56	+0.2	-0.2	+2.6	-2.7
WH	0.67	+0.2	-0.6	+3.5	-3.5
ZH	0.38	+1.6	-1.5	+3.6	-3.6
ttH	0.13	+3.8	-9.3	+7.8	-7.8

Table 4: Systematic uncertainty on the number of fitted signal events due to the background model for the $\sqrt{s}$ = 7 TeV (10 categories) and $\sqrt{s}$ = 8 TeV (14 categories) analyses. Three different background models are used depending on the category; an exponential function, a fourth order polynomial and the exponential of a second order polynomial.

Category	Parametrisation	Uncertainty [N_{evt}]	
		$\sqrt{s}$ = 7 TeV	$\sqrt{s}$ = 8 TeV
Inclusive	4th order pol.	7.3	12.0
Unconverted central, low p_{Tt}	Exp. of 2nd order pol.	2.1	4.6
Unconverted central, high p_{Tt}	Exponential	0.2	0.8
Unconverted rest, low p_{Tt}	4th order pol.	2.2	11.4
Unconverted rest, high p_{Tt}	Exponential	0.5	2.0
Converted central, low p_{Tt}	Exp. of 2nd order pol.	1.6	2.4
Converted central, high p_{Tt}	Exponential	0.3	0.8
Converted rest, low p_{Tt}	4th order pol.	4.6	8.0
Converted rest, high p_{Tt}	Exponential	0.5	1.1
Converted transition	Exp. of 2nd order pol.	3.2	9.1
Loose high-mass two-jet	Exponential	0.4	1.1
Tight high-mass two-jet	Exponential	-	0.3
Low-mass two-jet	Exponential	-	0.6
$E_{\text{T}}^{\text{miss}}$ significance	Exponential	-	0.1
One-lepton	Exponential	-	0.3

Table 5: Summary of the impact of systematic uncertainties on the signal yields for the analysis of the 8 TeV data.

Systematic uncertainties	Value(%)			Constraint
Luminosity	±3.6			
Trigger	±0.5			
Photon Identification	±2.4			Log-normal
Isolation	±1.0			
Photon Energy Scale	±0.25			
Branching ratio	±5.9% − ±2.1% (m_H = 110 - 150 GeV)			Asymmetric Log-normal
Scale	ggF: $^{+7.2}_{-7.8}$	VBF: $^{+0.2}_{-0.2}$	WH: $^{+0.2}_{-0.6}$	Asymmetric
	ZH: $^{+1.6}_{-1.5}$	ttH: $^{+3.8}_{-9.3}$		Log-normal
PDF+α_s	ggF: $^{+7.5}_{-6.9}$	VBF: $^{+2.6}_{-2.7}$	WH: ±3.5	Asymmetric
	ZH: ±3.6	ttH: ±7.8		Log-normal
Theory cross section on ggF	Tight high-mass two-jet:		±48	Log-normal
	Loose high-mass two-jet:		±28	
	Low-mass two-jet:		±30	

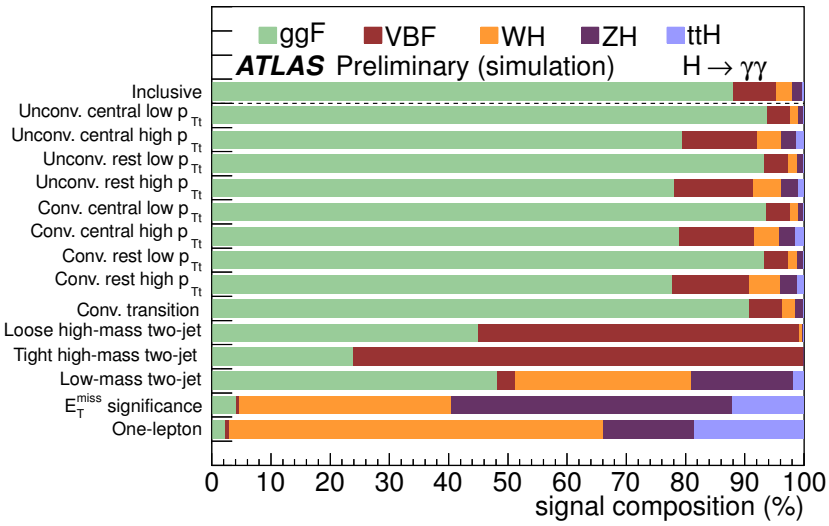

Figure 9: Decomposition of the expected signal from the various production processes for each category at m_H = 126.5 GeV for $\sqrt{s}$ = 8 TeV.

Table 6: Systematic uncertainties on the signal assignment to categories (migration) for the analysis of the 8 TeV data.

Systematic uncertainties	Category		Value(%)		Constraint
Underlying Event	Tight high-mass two-jet	ggF: ±8.8	VBF: ±2.0	VH, ttH: ±8.8	Log-normal
	Loose high-mass two-jet	ggF: ±12.8	VBF: ±3.3	VH, ttH: ±12.8	
	Low-mass two-jet	ggF: ±12	VBF: ±3.9	VH, ttH: ±12	
Jet Energy Scale	Low p_{Tt}	ggF: −0.1	VBF: −1.0	Others: −0.1	Gaussian
	High p_{Tt}	ggF: −0.7	VBF: −1.3	Others: +0.4	
	Tight high-mass two-jet	ggF: +11.8	VBF: +6.7	Others: +20.2	
	Loose high-mass two-jet	ggF: +10.7	VBF: +4.0	Others: +5.7	
	Low-mass two-jet	ggF: +4.7	VBF: +2.6	Others: 1.4	
	$E_{\mathrm{T}}^{\mathrm{miss}}$significance	ggF: 0.0	VBF: 0.0	Others: 0.0	
	one-lepton	ggF: 0.0	VBF: 0.0	Others: −0.1	
Jet Energy Resolution	Low p_{Tt}	ggF: 0.0	VBF: 0.2	Others: 0.0	Gaussian
	High p_{Tt}	ggF: −0.2	VBF: 0.2	Others: 0.6	
	Tight high-mass two-jet	ggF: 3.8	VBF: −1.3	Others: 7.0	
	Loose high-mass two-jet	ggF: 3.4	VBF: −0.7	Others: 1.2	
	Low-mass two-jet	ggF: 0.5	VBF: 3.4	Others: −1.3	
	$E_{\mathrm{T}}^{\mathrm{miss}}$significance	ggF: 0.0	VBF: 0.0	Others: 0.0	
	one-lepton	ggF: −0.9	VBF: −0.5	Others: −0.1	
η^* modelling	Tight high-mass two-jet: +7.6				Gaussian
	Loose high-mass two-jet: +6.2				
Dijet angular modelling	Tight high-mass two-jet: +12.1				Gaussian
	Loose high-mass two-jet: +8.5				
Higgs p_{T}	Low p_{Tt}: +1.3				Gaussian
	High p_{Tt}: −10.2				
	Tight high-mass two-jet: −10.4				
	Loose high-mass two-jet: −8.5				
	Low-mass two-jet: −12.5				
	$E_{\mathrm{T}}^{\mathrm{miss}}$significance: −2.0				
	one-lepton : −4.0				
Material Mismodelling	Unconv: −4.0		Conv: +3.5		Gaussian
JVF	Loose High-mass two-jet	ggF: −1.2	VBF: −0.3	Others: −1.2	Gaussian
	Low-mass two-jet	ggF: −2.3	VBF: −2.4	Others: −2.3	
$E_{\mathrm{T}}^{\mathrm{miss}}$	$E_{\mathrm{T}}^{\mathrm{miss}}$significance	ggF: +66.4	VBF: +30.7	VH, ttH: +1.2	Gaussian
e reco and identification	one-lepton: < 1				Gaussian
e Escale and resolution	one-lepton: < 1				Gaussian
μ reco, ID resolution	one-lepton: < 1				Gaussian
μ spectrometer resolution	one-lepton: 0				Gaussian

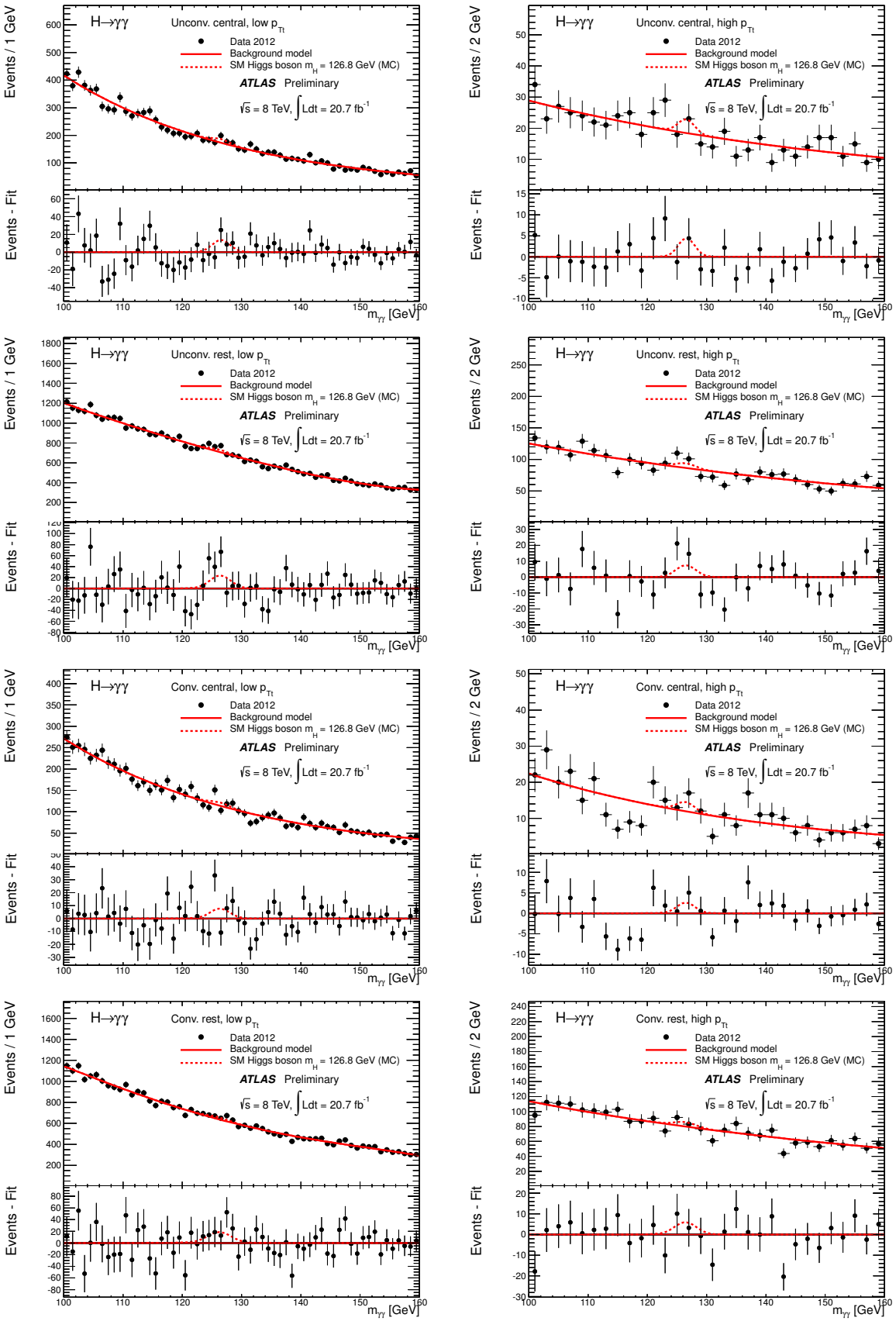

Figure 10: Background-only fits to the diphoton invariant mass spectra for categories. The bottom inset displays the residual of the data with respect to the background fit. The Higgs boson expectation for a mass hypothesis of 126.8 GeV corresponding to the SM cross section is also shown.

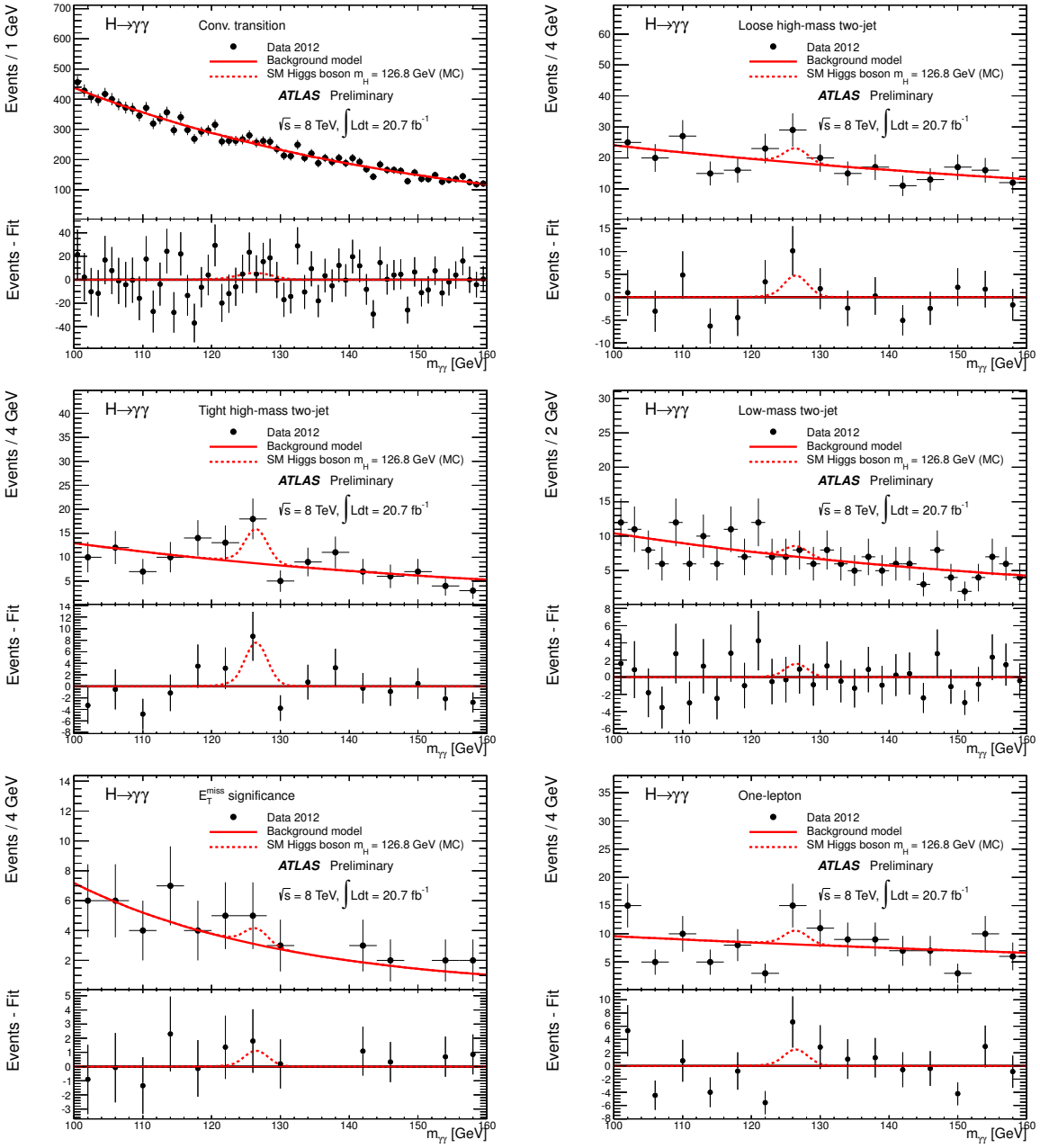

Figure 11: Background-only fits to the diphoton invariant mass spectra for categories. The bottom inset displays the residual of the data with respect to the background fit. The Higgs boson expectation for a mass hypothesis of 126.8 GeV corresponding to the SM cross section is also shown.

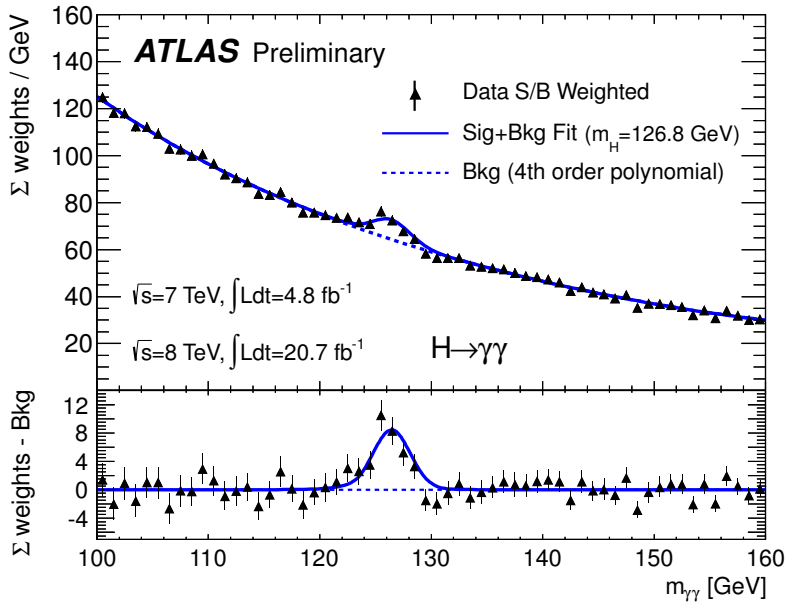

Figure 12: The weighted distribution of the invariant mass of diphoton candidates for the combined 7 TeV and 8 TeV data samples. The weight w_i for category i from [1, 14] is defined to be $ln(1 + S_i/B_i)$, where S_i is the expected number of signal events in a mass window that contains 90% of the signal events, and B_i is the integral in the same window of a background-only fit.

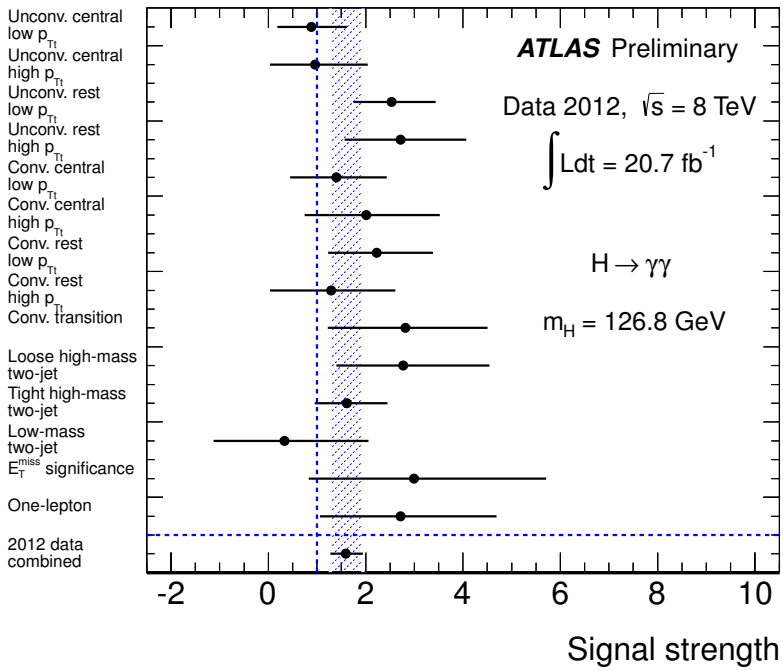

Figure 13: The observed signal strength μ for the 14 categories of the 8 TeV data analysis.

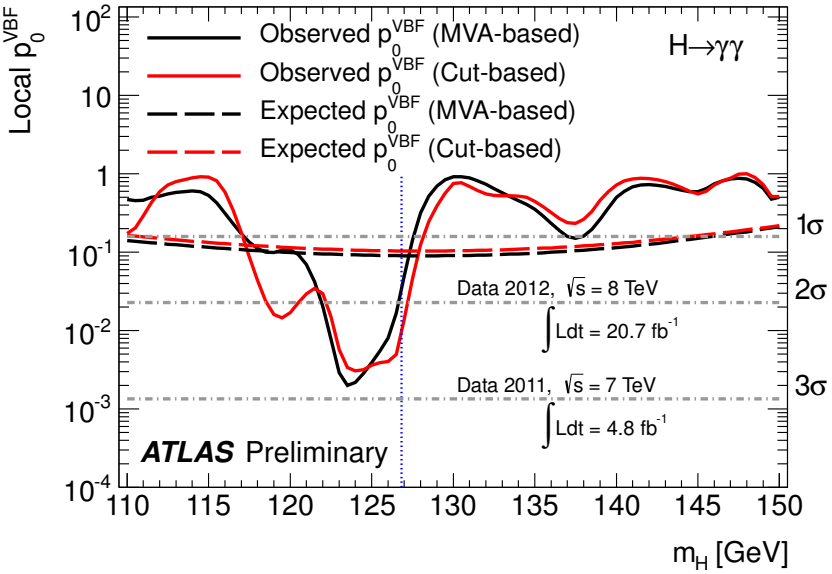

Figure 14: The observed local p_0^{VBF} value for VBF production as a function of m_H for the combination of $\sqrt{s} = 7$ TeV and $\sqrt{s} = 8$ TeV data (solid line) and the corresponding expected local p_0^{VBF} values for the SM Higgs boson signal plus background hypothesis (dashed line). In parallel to the baseline MVA analysis, the cut based selection described in Ref. [6] was re-optimised: two categories are defined, with more or less stringent cuts. The "tight high-mass two-jets" category is defined by $\Delta\eta_{jj} > 2.4$, $m_{jj} > 520$ GeV, $\Delta\phi_{\gamma\gamma;jj} > 2.6$, $\eta^* < 2.4$ and $\Delta R^{\gamma j}_{\rm min} > 2$. Events failing those cuts but passing the ones used in Ref. [6] enter into the "loose high-mass two-jets" category. Both the baseline MVA analysis and the reoptimised cut based analysis are shown.

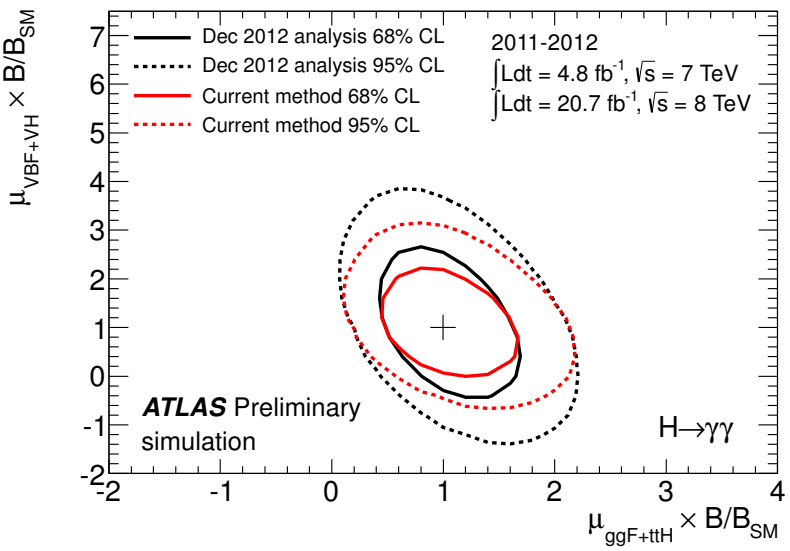

Figure 15: The SM expected best-fit values (+) of $\mu_{ggF+ttH} \times B/B_{SM}$ and $\mu_{VBF+VH} \times B/B_{SM}$ and their 68% (solid) and 95% (dashed) CL contours. The red lines correspond to the contours with the method described in this note (14 categories) and the black lines to the contours with the method described in Ref. [6] (12 categories), for the same integrated luminosity. The uncertainty on the μ_{VBF+VH} coupling measurement is reduced by the redefinition of the categories enriched in VBF and VH process events.

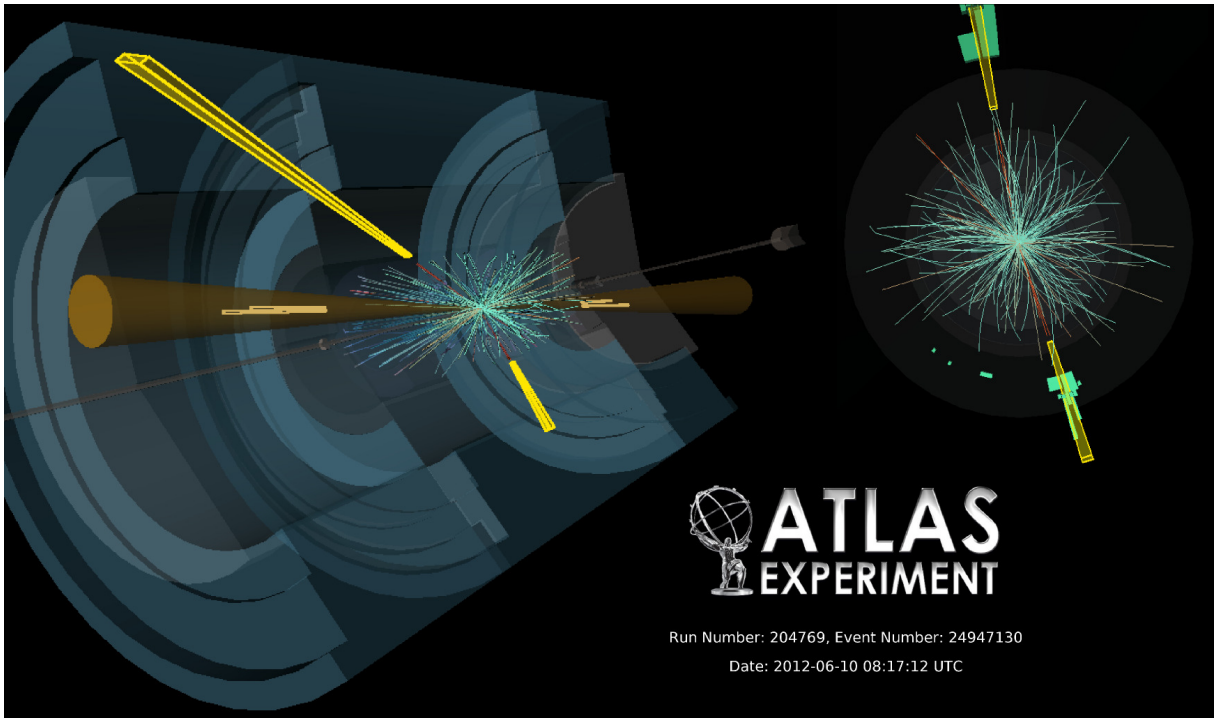

Figure 16: Event display of a VBF $H \to \gamma\gamma$ candidate, containing two converted photons and two high-mass jets. The event was recorded at $\sqrt{s} = 8$ TeV. The leading photon has $E_{\mathrm{T}} = 80.1$ GeV and $\eta = 1.01$. The subleading photon has $E_{\mathrm{T}} = 36.2$ GeV and $\eta = 0.17$. The measured diphoton mass is 126.9 GeV. The p_{T} and p_{Tt} of the diphoton system are 44.3 GeV and 6.2 GeV, respectively. The leading jet has $E_{\mathrm{T}} = 121.6$ GeV and $\eta = -2.90$. The subleading jet has $E_{\mathrm{T}} = 82.8$ GeV and $\eta = 2.72$. The measured two-jet mass is 1.67 TeV. The $\Delta\phi$ between the diphoton system and the system of the two-jet is 2.90.

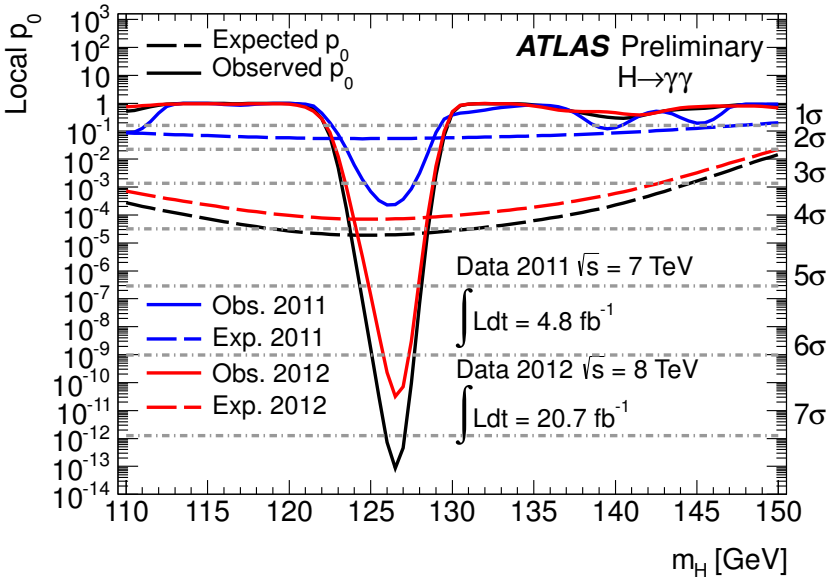

Figure 17: The observed local p_0 value as a function of m_H for the $\sqrt{s} = 7$ TeV data (blue), $\sqrt{s} = 8$ TeV data (red), and their combination (black). The expected local p_0 under the SM Higgs boson signal plus background hypothesis is shown in dashed curves. The largest local significance in the combination of $\sqrt{s} = 7$ TeV data and $\sqrt{s} = 8$ TeV data is found to be 7.4 σ at $m_H = 126.5$ GeV, where the expected significance is 4.1 σ.

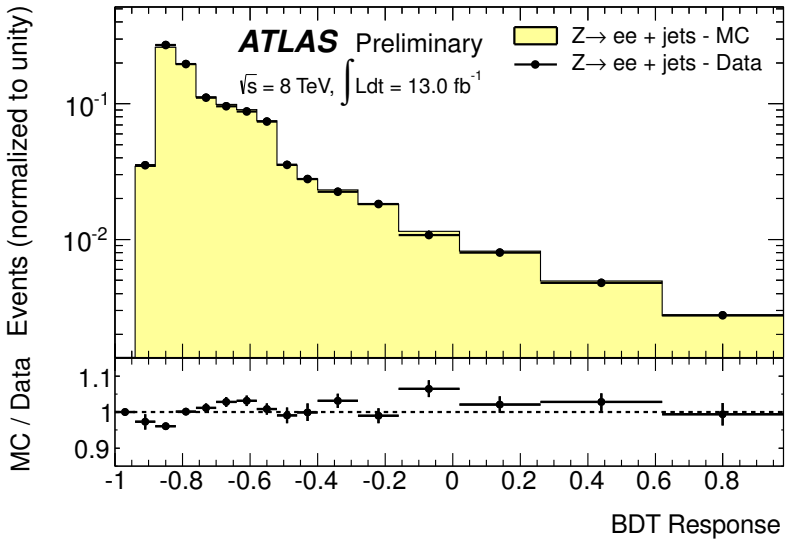

Figure 18: BDT response for $Z \to ee$+jet events in data and SHERPA MC and their ratio. Events are required to have $84 < m_{ee} < 96$ GeV and at least two jets. Electrons are taken as photons for the BDT input variables.